

Review

Graphene-Based Nanomaterials for Photothermal Therapy in Cancer Treatment

Daniela F. Báez ^{1,2} ¹ Escuela de Medicina, Universidad de Talca, Talca 3460000, Chile; daniela.baez@utalca.cl² Instituto de Investigación Interdisciplinaria, Vicerrectoría Académica, Universidad de Talca, Talca 3460000, Chile

Abstract: Graphene-based nanomaterials (GBNMs), specifically graphene oxide (GO) and reduced graphene oxide (rGO), have shown great potential in cancer therapy owing to their physicochemical properties. As GO and rGO strongly absorb light in the near-infrared (NIR) region, they are useful in photothermal therapy (PTT) for cancer treatment. However, despite the structural similarities of GO and rGO, they exhibit different influences on anticancer treatment due to their different photothermal capacities. In this review, various characterization techniques used to compare the structural features of GO and rGO are first outlined. Then, a comprehensive summary and discussion of the applicability of GBNMs in the context of PTT for diverse cancer types are presented. This discussion includes the integration of PTT with secondary therapeutic strategies, with a particular focus on the photothermal capacity achieved through near-infrared irradiation parameters and the modifications implemented. Furthermore, a dedicated section is devoted to studies on hybrid magnetic-GBNMs. Finally, the challenges and prospects associated with the utilization of GBNM in PTT, with a primary emphasis on the potential for clinical translation, are addressed.

Keywords: graphene oxide; reduced graphene oxide; graphene-based nanomaterials; photothermal therapy; magnetic iron oxide nanoparticles; cancer



Citation: Báez, D.F. Graphene-Based Nanomaterials for Photothermal Therapy in Cancer Treatment. *Pharmaceutics* **2023**, *15*, 2286. <https://doi.org/10.3390/pharmaceutics15092286>

Academic Editors: Xiaowei Zeng, Marta Laranjeira and Fernando J. Monteiro

Received: 11 June 2023

Revised: 17 August 2023

Accepted: 31 August 2023

Published: 6 September 2023



Copyright: © 2023 by the author. Licensee MDPI, Basel, Switzerland. This article is an open access article distributed under the terms and conditions of the Creative Commons Attribution (CC BY) license (<https://creativecommons.org/licenses/by/4.0/>).

1. Introduction

Cancer is among the leading causes of death worldwide [1]. The conventional treatments for this disease include surgical resection of the tumor, hormonal therapy, radiotherapy, and chemotherapy with a combination of drugs. However, most of these strategies induce adverse reactions with varying degrees of severity in patients or low effectiveness when the disease is in advanced stages [2]. Consequently, researchers are constantly searching for noninvasive anticancer strategies. Photothermal therapy (PTT) has attracted widespread attention due to its excellent therapeutic efficacy in locally treating different types of cancer. PTT is promoted by materials termed photothermal agents (PTAs) that absorb and convert near-infrared (NIR) light into heat; this heat generates sufficient temperature to cause hyperthermia, which can induce the death of cancer cells [3–5]. As depicted in Figure 1, the therapeutic approach with PTT entails several sequential steps. First, a targeted PTA is administered to the tumor site. Then, NIR irradiation is locally applied to the affected area to excite the surface plasmons of the PTA, causing the absorbed energy to be converted into heat through nonradiative relaxation. Subsequently, the temperature rises, leading to hyperthermia, which selectively targets and destroys cancer cells [6–9].

A key feature of PTT is that the applied NIR irradiation must induce high photothermal conversion to produce a temperature greater than 42 °C and cause hyperthermia in the damaged zone [10]. This process becomes challenging when tumors are located deep within tissues, such as in lung, pancreatic, colorectal, and stomach tissues, or when the disease has spread throughout the body. To overcome these limitations, researchers have combined PTT with a second therapeutic strategy to improve the therapeutic effect and used nanomaterials with

strong absorption of NIR light to increase the photothermal conversion [11–13]. Reports of these strategies have been well documented, with a focus on cancer therapy and the nature, shape, and size of the different nanomaterials applied [9,11,14–19].

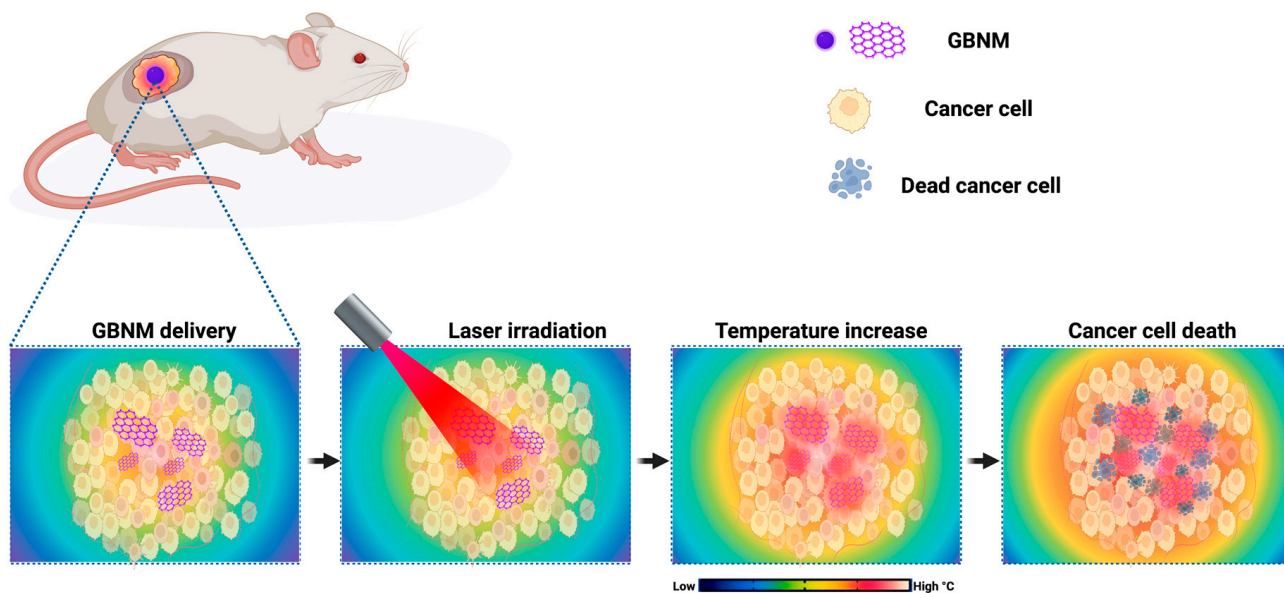


Figure 1. Schematic illustration of photothermal therapy for cancer treatment. This figure is original for this work. Created with [BioRender.com](https://www.biorender.com).

Several nanomaterials exhibit remarkable NIR-absorbing capabilities from the first NIR window (NIR-I, 750–1000 nm) or second NIR window (NIR-II, 1000–1500 nm), including noble and transition metal nanoparticles [20], carbon nanotubes [21,22], and graphene-based nanomaterials (GBNMs) [23]. Among them, gold nanoparticles have been extensively studied as PTAs and have demonstrated good biocompatibility and low toxicity. However, their ability to perform photothermal conversion is influenced by the morphology, size, and specific wavelength used for the irradiation [24]. GBMNs, specifically graphene oxide (GO) and reduced graphene oxide (rGO), are 2D materials that have shown great potential in cancer therapy. Due to the outstanding physicochemical properties of GO and rGO, these materials have been applied in biosensing and in the treatment of different types of cancer [25].

The applications of GO and rGO in PTT have recently been well reviewed because these materials exhibit strong absorbance in the NIR region. These reports focused on their functionalization, their toxicity, and the type of cancer treated. Nevertheless, comparisons between the photothermal capacity of GO and rGO have been limited [11,23,25–29].

This review focuses on providing a comparative analysis of the photothermal capacity of GO and rGO for the therapy of different types of cancer. In the following sections, a comparative overview of GO and rGO structural features is presented through different characterization techniques. Then, the utility of GO/rGO-based systems for single photothermal and combined photothermal therapy of different types of cancer is analyzed. Emphasis was placed on the photothermal conversion obtained according to the NIR wavelength, the type of GBMNs, the modification performed, and the secondary therapy used. After that, a special section is dedicated to hybrids between GBNM and magnetic iron nanoparticles, particularly magnetite and maghemite, as these materials can potentially be manipulated by applying an external magnetic field; thus, these materials could be guided and used as photothermal agents [30,31].

Finally, challenges and prospects are discussed regarding the application of GBMNs for photothermal therapy and potential clinical use.

2. Graphene-Based Nanomaterials

2.1. Structural Features of Graphene-Based Nanomaterials

Graphene oxide and reduced graphene oxide are the two main kinds of graphene-based nanomaterials within the family of carbon nanomaterials [32–34]. Both GBNMs exhibit exceptional properties and high biocompatibility owing to their composition and structural features; as a result, the GBNMs are used in many biomedical applications [23].

GO and rGO share similarities, as shown schematically in Figure 2. They are a 2D one-atom-thick layer that is composed of carbon atoms arranged in a honeycomb lattice with a network of delocalized π electrons. However, despite these similarities, their structures exhibit differences that affect their properties. For instance, GO is commonly synthesized through the Hummers and Offeman method [35], which consists of oxidizing graphite with a strongly acidic solution under controlled reaction conditions. Then, the oxidized graphite is subjected to a mechanical process that allows its interaction with water molecules, which intercalate and separate the sheets into random sizes to generate graphene oxide. Thus, the structure of graphene oxide changes from the original honeycomb lattice of graphite to a network of sp^2 and sp^3 hybridized carbon atoms and several oxygen functional groups, such as hydroxy, epoxy, and carboxy groups [36]. In contrast, rGO is obtained by reducing the oxygen functional groups in graphene oxide and restoring the sp^2 network to a similar graphene-like structure [37]. Chemical, thermal, hydrothermal, and electrochemical methods are the most commonly used techniques to reduce GO [37]. However, depending on the chosen reduction method, different carbon, oxygen, and intrinsic defect degrees are obtained.

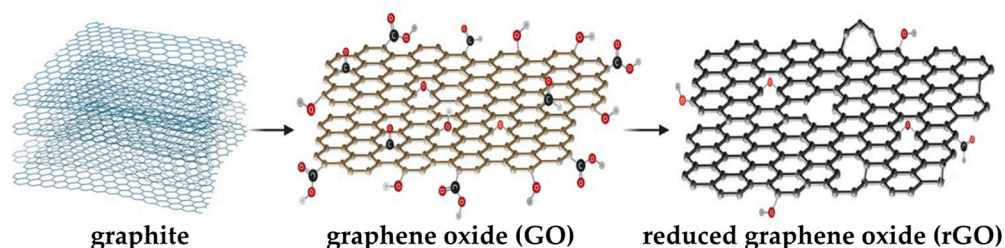


Figure 2. Schematic illustration of graphite, graphene oxide, and reduced graphene oxide structures. This figure is original for this work. Created with [BioRender.com](https://www.biorender.com).

Compared with GO, rGO exhibits greater electrical conductivity, which is particularly beneficial for the development of electrochemical biosensors [33,38]. However, rGO is highly hydrophobic and poorly dispersed in aqueous solutions; thus, the loading of molecules is usually achieved through noncovalent interactions, i.e., π - π and electrostatic interactions. As a result, drug administration must be carefully considered due to the possibility of desorption in non-target areas. Conversely, GO is more hydrophilic than rGO, disperses better in water, and can be functionalized with various biomolecules through covalent or noncovalent interactions, making it an excellent drug carrier [39,40].

2.2. Structural Characterization of Graphene-Based Nanomaterials

The differences in properties between GO and rGO are mainly attributed to their composition and structure. Various characterization techniques, such as X-ray photoelectron spectroscopy (XPS), Raman spectroscopy, transmission electron microscopy (TEM), X-ray diffraction (XRD), and UV-NIR spectrophotometry, are commonly employed to determine the structure of GO and to assess the degree of reduction when rGO is formed.

2.2.1. X-ray Photoelectron Spectroscopy (XPS)

The chemical composition of GO and rGO can be analyzed through X-ray photoelectron spectroscopy. Figure 3A(a,b) display the wide-scan spectra of GO and rGO, respectively. By examining the carbon and oxygen intensities, the effectiveness of a reduction method can be determined based on the C/O or O/C ratios [41–44]. A higher C/O or lower O/C ra-

tio indicates a less prominent oxygen peak and a better reduction of oxygen functionalities to form rGO. In this regard, the atomic O/C ratio for GO was higher than that for rGO, as expected. Figure 3B(a) shows high-resolution C 1s spectra for GO that present four distinct contributions related to the functional groups due to oxidation. The contribution located at 284.6 eV are associated with the C–C/C=C groups, whereas those observed at 286.8 eV, 288.2 eV, and 289.2 eV correspond to the C–O, C=O, and O–C=O groups, respectively. The C 1s spectra of rGO are presented in Figure 3B(b). An additional contribution was needed to accurately fit the experimental data at 286.1 eV, which is associated with the C–OH groups. Additionally, a broad π – π^* satellite peak was observed at approximately 291.2 eV [45].

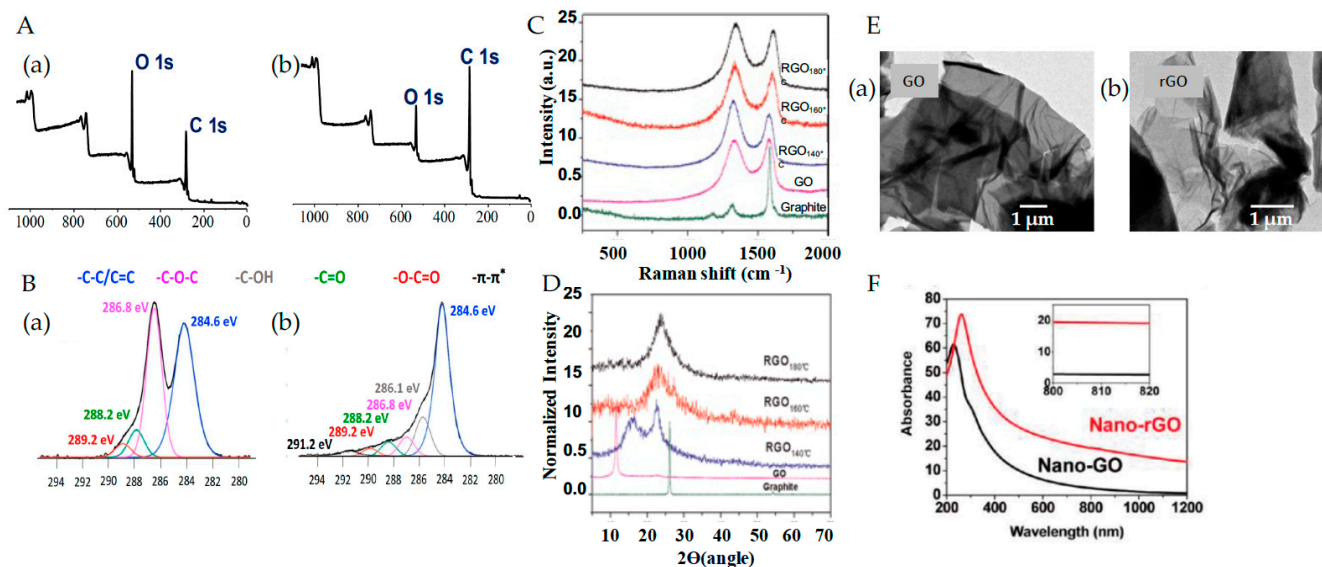


Figure 3. (A) X-ray photoelectron spectroscopy (XPS): wide scan recorded from (a) GO and (b) rGO. (B) XPS: C 1s spectra for (a) GO and (b) rGO. (C) Raman spectra of graphite (green), GO (purple), and rGO (black, red, and blue). (D) XRD patterns of graphite (green), GO (purple), and rGO (blue, red, and black). (E) TEM images of (a) GO and (b) rGO. (F) UV-vis absorption curves of nanoGO (black) and nanorGO (red). The inset shows a magnified view of the curves in the 800 nm region. (A,B) were adapted from Ref. [45] Copyright 2017 Nanomaterials. (C–E) were adapted from [46] Copyright 2014 Elsevier. (F) was adapted from [47] Copyright 2011 American Chemical Society.

2.2.2. Raman Spectroscopy

Raman spectroscopy is a nondestructive technique that characterizes the structure and quality of GBNMs. The most distinctive Raman modes observed for GBNMs are the D band (1324–1346 cm⁻¹) and the G band (1490–1691 cm⁻¹). The formation of the D-band results from the disruption of the graphitic sp² backbone, and its intensity is related to the number of defect sites. Figure 3C (green curve) shows the Raman spectra obtained for pristine graphite, which displays a characteristic prominent G peak at 1585 cm⁻¹ and a very weak D peak at approximately 1322 cm⁻¹ caused by the graphite edges, indicating that the graphite structure is very regular. The Raman spectra for GO are exhibited in Figure 3C (pink curve) and present a D band at approximately 1332 cm⁻¹ and a G band at 1579 cm⁻¹. The D band is very prominent compared with that observed for graphite, indicating that the defects increase after oxidation. This is due to changes in the hybridization from sp² to sp³ carbon atoms. A relationship between the intensities of the D and G bands (ID/IG ratio) is frequently used to quantify the degree of defects, and the ID/IG ratio of GO is higher than that of graphite. After the reduction process, the D band intensity continues to grow with respect to the G band (Figure 3C; blue, red, and black curve), and the ID/IG ratio indicates a significant degree of structural disorder from GO to rGO [46].

2.2.3. X-ray Diffraction (XRD)

The X-ray diffraction patterns obtained for graphite, GO, and rGO are shown in Figure 3D. The XRD pattern of graphite powder (Figure 3D, green curve) shows a sharp main diffraction peak at $2\theta = 26.50^\circ$, indicative of an interlayer distance of 0.34 nm. For GO (Figure 2G; pink curve), a complete pattern disappearance of the sharp feature peak can be observed, and a new broad peak appears near 10.27° (d-spacing 0.86 nm). The increase in the interlayer distance is due to the incorporation of oxygenated functionalities during the oxidation process and to the intercalation of water molecules between the new hydrophilic GO sheets. For rGO (Figure 3D; blue, red, and black curves), a dramatic change in 2θ angles can be observed. A broad and intense peak at 24.57° (d-spacing 0.36 nm) is obtained as a result of the reduction process, suggesting that the graphitic structure is restored. However, the width of the peak indicates that rGO shows a poorer crystalline character than graphite [46].

2.2.4. Transmission Electron Microscopy (TEM)

TEM is commonly employed to analyze the morphology of GBNMs. Figure 3E(a,b) show TEM images obtained for GO and rGO, respectively. Dark and large nanosheets were observed for GO, indicating some superposed layers, while transparent, wrinkled and folded structures were observed for rGO, indicating single-layer sheets [46].

2.2.5. Ultraviolet–Visible–Near-Infrared Spectrophotometry (UV–VIS–NIR)

The UV–VIS–NIR spectrophotometry technique is used to study the optical absorption properties of GO and rGO. Figure 3F shows the UV–VIS–NIR absorption spectrum obtained for GO (black curve) and rGO (red curve), in which a characteristic absorption peak at 228 nm is observed for GO. This peak is associated with π – π^* transitions of aromatic C–C bonds and a small shoulder at approximately 310 nm due to the n – π^* transitions of C=O bonds. In the case of rGO, a redshift in the absorption spectrum of this peak is observed, with a peak at approximately 265 nm, due to the decrease in oxygen functional groups and the increase in aromaticity upon successful reduction. In addition, the rGO band shows broad absorption throughout the visible region and a remarkable increase in the NIR absorbance compared with that of GO, indicating that rGO presents a superior capacity to absorb NIR light [47]. The presence of oxygen functional groups and defects in the structure of GO and rGO enables the absorption of NIR light, the excitation of surface plasmons, and the generation of heat by nonradiative relaxation. Taken together, these factors constitute the photothermal effect [48].

3. GBNMs for Photothermal Cancer Therapy

To date, several GO/rGO-based systems have been explored with the aim of producing a large photothermal effect for the treatment of cancer [27]. Factors such as the duration and intensity of external laser irradiation, as well as the modification and concentration of the GBNMs, have been considered, depending on the type of cancer treated. This section summarizes the application of GO and rGO in single or combined photothermal therapy according to the type of cancer treated.

3.1. Breast Cancer

Breast cancer is an aggressive disease that frequently results in metastasis, which spreads the disease to surrounding tissues [49]. To improve the treatment efficiency for this cancer, researchers have combined chemotherapy and photothermal therapy into one system. For instance, Zhang et al. combined chemotherapy and PTT by modifying nanoGO with doxorubicin and PEG to create NGO-PEG-DOX. A significant increase in the temperature from approximately 26 °C to 50 °C was observed when EMT6 tumor samples were treated with NGO-PEG-DOX for 3 min under NIR irradiation (808 nm laser + 2 W/cm²). The inhibition rate was superior when the modified GO was used at 10 mg/mL DOX and NIR irradiation in comparison to that of free DOX and NGO-PEG. The authors attributed

the enhanced cell-killing effect to the hastened DOX release from NGO-PEG at elevated temperatures and the increasing heat sensitivity of cells. The *in vivo* results demonstrated that when mice were treated only with DOX, the volume of their tumors rapidly grew. For mice treated with NGO-PEG without DOX and 2 W/cm² NIR laser for 5 min, the tumor volume was reduced in the first week, but the tumor began to grow again. On the other hand, four out of five mice in the NGO-PEG-DOX group achieved total tumor ablation 1 day after NIR irradiation, leaving black scars on the original tumor sites. Moreover, the tumors did not regrow within the next 40 days. These findings suggest that combining chemotherapy with locally external NIR photothermal therapy could be a promising treatment option for patients with breast cancer [50]. Similar results were described by Zhu et al., who developed a thermosensitive hydrogel based on chitosan and graphene oxide loaded with docetaxel (DTX-GO/CS). When the DTX-GO/CS gel was used in combination with NIR laser irradiation (at 808 nm and 2.5 W), this was found to exhibit a higher inhibition rate in MCF-7 cells than that achieved without NIR irradiation. In addition, the effectiveness of DTX-GO/CS in reducing tumor growth was observed in S180 tumor-bearing mice after 12 days of treatment. The results revealed that compared with other control methods, the application of the nanosystem in combination with NIR irradiation resulted in a significant reduction in tumor volume and weight, suggesting that the nanosystem can effectively inhibit tumor growth [51]. The synergistic combination of PTT and photodynamic therapy (PDT) as a second therapeutic strategy has also been studied, showing that the tumor temperature reached almost 50 °C after 3 min of laser exposure when using a nanographene oxide sheet modified with the Pluronic block copolymer and complexed with methylene blue (Figure 4A,B). Tumor tissues were completely burned without mass detected on Day 3 (Figure 4C); however, a small tumor mass was observed on Day 6, and tumors started to regrow after Day 9, indicating that PTT was not enough to eradicate carcinogenic tissue. Therefore, PTT was combined with PDT. After 15 days of treatment, no tumor tissue was detected in any treated mice, indicating complete tumor regression. These results corroborate that combining PTT with a second therapy enhances *in vivo* cancer therapeutic efficiency [52].

The chemistry, morphology, and size of GBNMs can affect the photothermal conversion and, consequently, the results of photothermal therapy for cancer [53,54]. In this sense, Yang et al. compared the size and photothermal capacity of GO, chemically reduced GO, and their nanosized versions functionalized with C₁₈PMH-PEG. The size of the nanoGO-PEG sheets was much smaller than that of rGO-PEG and similar to that of the nanorGO-PEG sheets, with equivalent diameters of 23, 65, and 27 nm. However, the NIR absorption at 808 nm of nanorGO-PEG and rGO-PEG was 3–4-fold higher than that of nanoGO-PEG. On the other hand, the *in vivo* results obtained using a lower power density of 0.15 W/cm² and 5 min of laser irradiation showed that the surface temperature of mouse tumors treated with nrGO-PEG reached ~48 °C, while that of tumors treated with nGO-PEG only increased by 41 °C. Moreover, the latter conditions resulted in rapid tumor growth, indicating that the unreduced version in these conditions was not effective for the photothermal ablation of tumors [55]. Li et al. carried out a similar study but compared the size and oxidation degree of GO after successive modifications for integrated chemotherapy and PPT against 4T tumors (Figure 4D). Ultrafine GO nanosheets (UGO) presented a width of 30 nm with a thickness of 0.78 nm (Figure 4F(b)), which did not significantly change after DOX loading (Figure 4F(c); UD). However, a larger average lateral size (~50 nm) and thickness (9.8 nm) was observed when polydopamine coated the UD system (Figure 4F(d); UDP). The photothermal conversion profile shown in Figure 4G presented a similar rise in temperature for UGO and UD, which reached approximately 37 °C after NIR irradiation (808 nm, 1.5 W/cm², 300 s). The temperature increased dramatically when using UDP and reached approximately 50 °C, demonstrating that the enhanced photothermal effect was due to polydopamine rather than GO, even at ultrasmall sizes. Similar results were described by Hashemi et al., who showed that rGO was 3.2-fold stronger in absorbing light at 808 nm than GO. In the same study, another factor that influences photothermal

conversion was investigated. The photothermal performance showed that at different power intensities and concentrations for GO and rGO, the temperature increased as the power intensity used for both GBNMs increased. However, after 5 min of irradiation with a power density of 1.7 W/cm^2 in a $400 \mu\text{g/mL}$ GO suspension, the temperature increased to $46.2 \text{ }^\circ\text{C}$; in an rGO suspension 4 times less concentrated, the temperature increased to $42.7 \text{ }^\circ\text{C}$ [56]. Therefore, rGO is a more effective transducer for photothermal therapy.

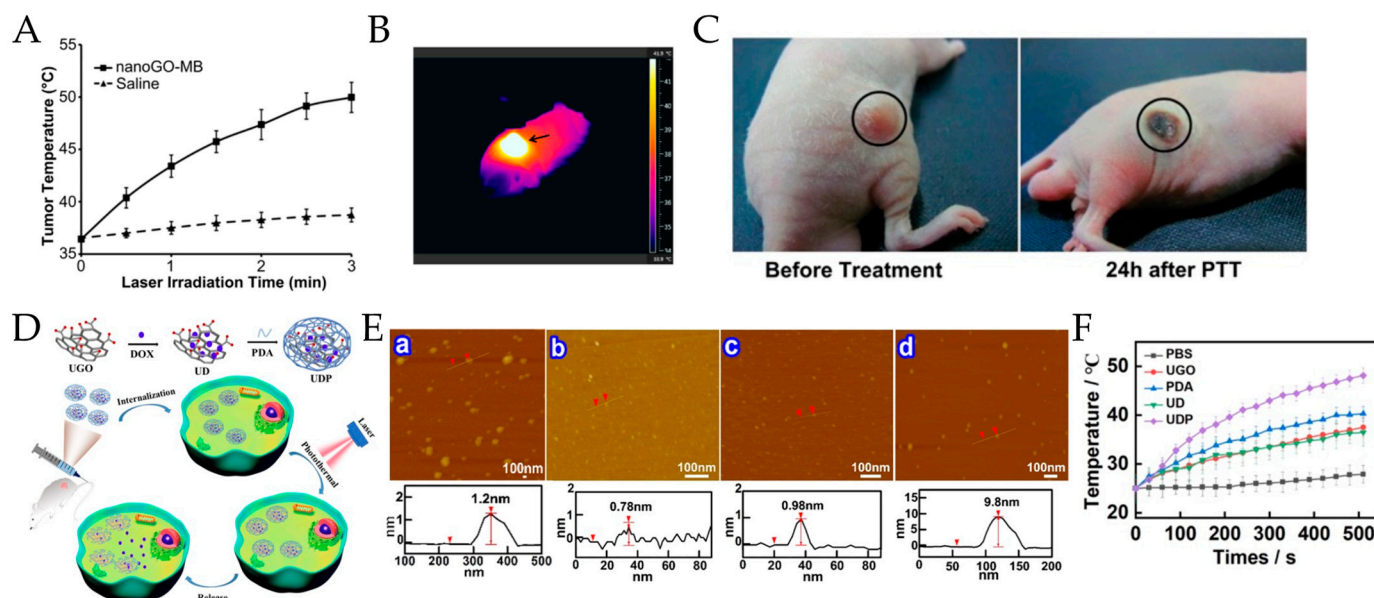


Figure 4. NIR-laser-induced photothermal effect of nanoGO in vivo. (A) The temperature change in tumor tissue after irradiation with an NIR laser (CW, 808 nm, 2 W/cm^2). (B) High temperature in the tumor (indicated by black arrow) at the time of photothermal treatment, showing a major temperature difference from the surrounding body as recorded by an IR camera. (C) The effect of photothermal treatment on the tumor tissue shows the burning and destruction of the tissue after 24 h of laser irradiation. Reproduced from [52] (Copyright: 2013, Elsevier). (D) Schematic illustration of the fabrication of UDP and the combination of enhanced chemotherapy and PTT against breast cancer in vivo. (E) AFM height images and section analysis of (a) PGO, (b) UGO, (c) UD, and (d) UDP. (F) The heating curve of PBS, UGO, PDA, UD, and UDP under NIR laser irradiation (808 nm, 1.5 W/cm^2 , 500 s). Adapted from [57] Copyright 2023, Elsevier.

Several hybrid combinations of GO with other NIR light-absorbing nanomaterials have been tested for their ability to increase the photothermal response. Gold nanoparticles, which exhibit optical properties, have been utilized in cancer therapy previously [20,58]. In this sense, Wang et al. integrated gold sphere nanoparticles with GO modified with an MUC1 aptamer and loaded them with DOX (GO-AuNP-Apt-DOX) for targeted chemotherapy and PTT. The photothermal conversion efficiency was determined by irradiating different concentrations (2.7, 5.3, and 8 mg/L) of the GO-AuNP solution at different times. The results showed a dose dependency and the highest temperature was $48 \text{ }^\circ\text{C}$. After exposure to NIR light, the release of DOX exceeded 80% within 2 h. In contrast, without irradiation, it only reached 40% after 7 h at $25 \text{ }^\circ\text{C}$. The results obtained from the cell viability analysis on the MCF7 cell line revealed that GO-Au-Apt caused more cell death than GO-AuNPs when exposed to NIR light. However, NIR irradiation did not result in increased cell death. The MCF7 cells exhibited a viability of 90% after 5 min of irradiation, but this value decreased rapidly to 80% as the irradiation time increased to 15 min [59]. Similar results have been obtained using polymers such as poly(allylamine hydrochloride) [60] and dopamine [61]. In the last study, Lima Sousa et al. evaluated the phototherapeutic capability of GO reduced with dopamine (P-DOPA-rGO) using 3D heterotypic spheroids. When spheroids were treated with P-DOPA-rGO and NIR irradiation (808 nm , 1.7 W/cm^2 ,

and 5 min), the temperature increased by approximately 36 °C. However, the viability decreased only to 30%, which was lower than the results obtained with monolayers of cancer cells (3%). The authors attributed this result to the spheroids' resistance to penetration or temperature-mediated death. These results suggest that a higher laser wavelength or concentration of the system may be necessary to reach the innermost part of this kind of 3D model tumor.

3.2. Lung Cancer

The photothermal agent concentration and the intensity of the laser power are key factors that affect the efficacy of photothermal therapy. In this sense, Du et al. investigated the temperature increase for an AS1411 aptamer and berberine-derivative graphene oxide-based system at different concentrations during NIR irradiation (808 nm and 2.5 W/cm²). The temperature at 128 µg/mL and 10 min irradiation reached 51.2 °C. In contrast, at 32 µg/mL, only 38.6 °C was achieved, confirming the concentration dependency. Then, the therapeutic efficacy of the combined chemo- and photothermal therapy was evaluated by treating A549 and L929 cell lines at different GO and AS1411-GO concentrations. For untreated A549 and L929 cells, irradiation for 3 min did not decrease cell viability, but when GO and AS1411-GO reached the highest concentration, the cell survival rates of A549 cells and L929 cells remained at approximately 98%, indicating that GO and AS1411-GO exhibited almost no cytotoxicity. The combined chemophotothermal therapy achieved an improved therapeutic effect with AS1411-GO/B3, as the survival rate of A549 cells reduced from 51% (without NIR irradiation) to 28% (with NIR irradiation) [62]. Wang et al. also assessed how much heat could be produced under exposure to NIR light under similar conditions to those in a previous report (808 nm, 2 W/cm², 5 min) but using different concentrations of rGO. The findings showed that as the concentration of rGO increased, the temperature also increased; at a concentration of 1 mg/mL and 5 min of irradiation, the temperature reached 50 °C, surpassing the photoablation temperature. In this case, the tumors from the A549 cell line treated with rGO decreased the cell viability sharply to 35% from 65% as the concentration increased [63]. In a different study, rGO was used in combination with mesoporous silica to form a sandwich structure modified with DOX (Figure 5A) in human lung cancer (A549) and human colorectal carcinoma (SW620) cell lines, and the results showed high viabilities of 84.7% with SW620 and 95.6% with A549, even at a concentration of 2.5 mg/mL. The synergistic chemophotothermal therapeutic effect was better when reduced GO (rGO@msilica) was used than when GO@msilica nanocarrier was used at a lower power intensity (0.3 W/cm² for 15 min using 808 nm laser light), which showed increased NIR absorption (Figure 5B) and a remarkable temperature increase (Figure 5C) of 14 °C compared with 4 °C, respectively [64].

3.3. Glioma

Deep cancerous tumors, such as glioma, need to be irradiated with high-intensity light to produce hyperthermia, especially when the first NIR window is used as the source of irradiation light. In a study by Dong et al., a higher power intensity of 2.5 W/cm² with a laser wavelength of 808 nm was used for combined chemophotothermal therapy. The viability of the C6 and BMVE cell lines remained above 95%, even at 100 µg/mL GO, indicating that GO is a safe nanocarrier for drug delivery. The *in vivo* results showed that using PEG- and DOX-based systems loaded with transferrin increased the head temperature of glioma-bearing rats by 4 °C (from 34.15 to 38.10 °C) in the focal region; this resulted from the heat conversion generated by the NIR-absorbing TPGD. By the end of the study, the median survival time of the TPGD+NIR group was significantly longer than that of the other groups (36 vs. 20 days) [5]. On the other hand, Robinson et al. used a laser of 808 nm at a very low power intensity (0.6 W/cm²) to irradiate different solutions of GO and its reduced version. As shown in Figure 5D, the temperature for GO remained below 36 °C after 8 min of irradiation for all the concentrations analyzed. However, when GO was reduced chemically to produce rGO (Figure 5E), the temperatures exceeded the

photoablation limit of 50 °C after 5 min of irradiation under the same experimental conditions [47]. This behavior has also been observed by other authors [33], such as Cheon et al., who developed DOX-loaded BSA-functionalized rGO (DOX-BSA-rGO) nanosheets for the chemophotothermal therapy of brain tumor cells. During testing, it was found that the temperature of GO did not change significantly when exposed to a 5.5 W/cm² NIR laser with a wavelength of 808 nm for 300 seconds. However, when BSA-rGO was used, the temperature exceeded 60 °C [31].

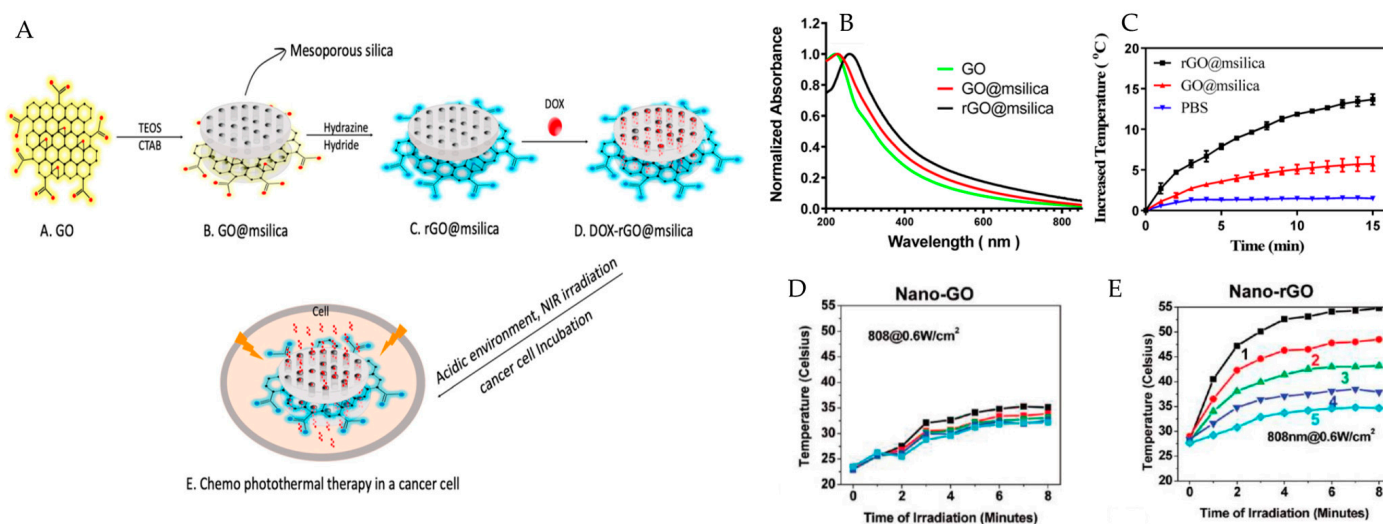


Figure 5. (A) Schematic illustration of a DOX-loaded rGO@msilica nanocarrier as a multifunctional drug delivery system for the synergistic chemophotothermal therapy of cancer. (B) Absorption spectra of GO, GO@msilica, and rGO@msilica nanocarriers. (C) Temperature-increasing curves of PBS, GO@msilica nanocarrier (0.5 mg/mL), and rGO@msilica nanocarrier (0.5 mg/mL) solutions exposed to an NIR laser (808 nm, 0.3 W/cm²) for 15 min. (D) Photothermal heating curves of nanoGO and nanorGO solutions. The black curve is 100 µL of solution with a 20 mg/L concentration of nanorGO or nanoGO; the red curve is 10 mg/L; the green curve is 5 mg/L; the dark blue curve is 2.5 mg/L; and the light blue curve is water. Panels A to C were adapted from [64] (Copyright 2020, American Chemical Society). (D,E) were adapted from [47] Copyright 2011, American Chemical Society.

It is evident that reducing GO leads to an enhanced photothermal capacity, regardless of the method applied. Various techniques have been devised for reducing GO [33,65], all of which leave residual oxygen groups and defects that remain in the structure [45]. However, the relationship between the method used to synthesize rGO and the photothermal capacity obtained has not been well researched. A chemical reduction, for instance, was performed on a GO nanomesh to produce the unreduced (GONM) and its reduced version (rGONM), suggesting that the reduction can provide more low-energy vibrational modes and higher NIR absorption; as a result, ultralow concentrations and lower laser power intensities could be used for PTT. As expected, the rGONM-PEG exhibited excellent photothermal heating under 808 nm of irradiation at low-power irradiation (0.1 W/cm²), reaching 50 °C after only 6 min of continuous irradiation. The in vivo results showed that the U87MG tumor was completely eliminated when 200 µL at 1 mg/mL per mouse (corresponding to a dose of ≈10 mg/kg) of rGONM-PEG-Cy7-RGD was injected and irradiated, without significant tumor regrowth and survival over 100 days [66].

3.4. Prostate Cancer

Prostate cancer is a silent and frequent cancer that is the fifth leading cause of cancer death among men [1]. To improve the detection and treatment of this disease, Zhang et al. designed and developed the GO/Bi₂Se₃/polyvinylpyrrolidone (GO/Bi₂Se₃/PVP) system by using the solvothermal method. Then, X-ray computed tomography and photoacoustic

(CT/PA) imaging combined with PTT was used to study the GO/Bi₂Se₃/PVP system. This study demonstrated that using an 808 nm laser at 0.4 W/cm², the temperature of a solution containing GO/Bi₂Se₃/PVP increased depending on the concentration and duration of laser irradiation exposure. After 5 min of irradiation, the temperature increased by up to 33 °C in a solution containing 150 µg/mL GO/Bi₂Se₃/PVP. The researchers believe that this enhanced photothermal effect was due to the in situ reduction of GO during the preparation [67]. A system similar to the previous one, in which a hybrid approach is used for multimodal imaging and photothermal therapy, was created using the solvothermal method. However, in this case, BaGdF₅ was used as the contrast agent. The temperature increase was 33 °C, achieved within 10 min at a concentration of 200 µg/mL [68].

A study conducted by Thapa et al. demonstrated that pegylated graphene oxide and a polar lipid liquid crystalline nanoparticle named monoolein (LCN) could potentially serve as a nanocarrier for docetaxel (PEG-GO/LCN/DTX) in chemophotothermal therapy. The system was subjected to high-intensity irradiation of 3 W/cm² for 3 min, which raised the temperature to 50 °C, resulting in increased cytotoxicity of the formulation. In vitro cell studies were carried out using DU145 prostate cancer cells, which are known for their DTX resistance and high metastatic potential. The results showed that the formulation exhibited high cellular uptake and inhibitory effects on the motility of DU145 cells [3]. SreeHarsha and colleagues also achieved similar outcomes using chitosan as a stabilizing matrix. They developed a nanocarrier system (HNP) that loaded DOX onto reduced graphene oxide. When PC-3 cell lines were treated with rGOD-HNP and irradiated, the toxicity was 2.53 times higher than that of rGOD-HNP without laser irradiation [69].

A more recent study examined a nanocarrier that uses macrophages as a biomimetic drug delivery system. This approach combined the natural function of macrophages with DOX, rGO, and NIR irradiation to destroy the macrophages and excrete DOX into the surrounding environment as a free drug. Figure 6A illustrates this process. Figure 6B(a) shows the photothermal conversion efficiency of MAs-DOX/PEG-BPEI-rGO, which produced a temperature of 55.8 °C 5 min after NIR irradiation is applied using an 808 nm laser (1 W/cm²) at 50 µg/mL. The study investigated the antitumor efficacy of this approach in tumor-bearing mice. The tumor temperature increased to 46.3 °C after treatment with MAs-DOX/PEG-BPEI-rGO (50 µg/mL PEG-BPEI-rGO) and NIR laser irradiation. Due to the good photothermal conversion efficiency of the rGO-based system, the growth of tumors (Figure 6B(b,c)) was significantly suppressed. In contrast, tumors in the group without NIR irradiation showed a growth rate similar to that in the control group. Furthermore, compared with the group treated with the same system without DOX but with irradiation, the group treated with MAs-DOX/PEG-BPEI-rGO and irradiation showed a better tumor inhibition effect [70].

Other hybrids have been formed with GO and rGO to improve photothermal conversion, including gold nanorods [71], graphene quantum dots [72], artesunate [73], and alginate [74], among others [75,76]. Table 1 summarizes the studies in which hybrids between GO/rGO and different materials with photothermal properties were used to improve the photothermal efficiency in the photothermal treatment of cancer. It is worth mentioning that many of these studies use laser light from the NIR-I window (mostly 808 nm) to induce hyperthermia. Although this wavelength is attractive because biological systems lack chromophores that absorb in this region, it is not very effective in treating tumors that are deep or sizable because its penetration depth in body tissues is limited; for that reason, higher power intensities are required. In this sense, the NIR-II window is a better option to use as a light source for irradiation because it can penetrate deeper into tissues due to less scattering with longer wavelengths. Additionally, higher power intensities can be used [48,77,78]. Therefore, when designing new strategies to treat cancer photothermally using GBNMs, researchers should consider the NIR-II region for irradiation.

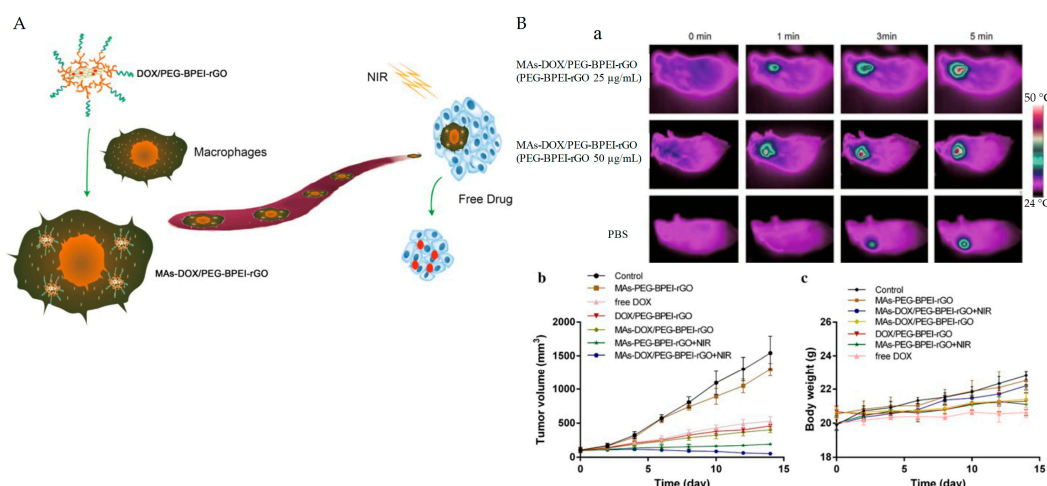


Figure 6. (A) Schematic illustration of macrophage loading with DOX/PEG-BPEI-rGO to target the tumor site and initiate drug release after NIR irradiation. (B) Thermographic images of tumor-bearing mice treated with PBS or MAs-DOX/PEG-BPEI-rGO 4 h after injection following NIR irradiation for 5 min (1 W/cm^2). (b) Relative tumor volume in different treatment groups ($n = 5$). (c) Changes in body weight in response to different treatments ($n = 5$). Adapted from [70] Copyright 2019, Lei Qiang et al., Springer Nature.

Table 1. Overview of GO/rGO Hybrids and their Application in Photothermal Cancer Therapy.

GBNM Hybrid System	Cell Line/Cancer Type	Irradiation Conditions	Temperature ($^{\circ}\text{C}$)	Reference
rGO@AuNS- DODAB/DOPE-FA	Pancreatic	808 nm; 0.1 W/cm^2	52.6	[79]
(PNIPAMAAM)/GO	hASCs and MDA-MB-231	808 nm; 4.0 W/cm^2	36	[80]
IR780-NGO-RSV	Ovarian	808 nm; 0.3 W/cm^2	61.5	[81]
Pd@PPy/GO	MCF-7	808 nm; 1.5 W/cm^2	30 (ΔT)	[82]
PTX@GO-PEG-OSA	Gastric cancer	808 nm; 1.0 W/cm^2	43	[83]
GO-FA/Ce6	MCF-7	808 nm; 2.0 W/cm^2	17 (ΔT)	[75]
nGO-PEG-ARS	HepG2	808 nm; 2.0 W/cm^2	60	[73]
fGO@GNRs-DOX	HeLa and A549	808 nm; 1.0 W/cm^2	59	[71]
GO-PEG-FA	Breast cancer	808 nm; 4.0 W/cm^2	68	[76]
GO-PEI-GQDs	MDA-MB-231	808 nm; 0.5 W/cm^2	48	[72]
AGD	A549	808 nm; -	50	[74]
GO+PEGFA+ICG	Ehrlich tumor	808 nm; 1.8 W/cm^2	40 (ΔT)	[84]
ICG@MS-rGO-FA	Colorectal	808 nm; 1.0 W/cm^2	26 (ΔT)	[85]
nGO-PEG	Colon	808 nm; 1.5 W/cm^2	47 (ΔT)	[86]
GO@SiO ₂ @AuNS	KM12C	808 nm; 0.3 W/cm^2	16 (ΔT)	[87]
nGO-COS-CD47/DTIC	Melanoma	808 nm; 2.0 W/cm^2	55	[88]
GO-v50-DOX	Melanoma	808 nm; 7.0 W/cm^2	54	[89]
rGO-AuNS, rGO-AuNR	HUVECs	808 nm; 3.0 W/cm^2	57 (ΔT)	[90]

Abbreviations: AuNS (gold nano star particle); DODAB/DOPE (bromide/1,2-dioleoyl-sn-glycero-3-phosphoethanolamine); RSV (resveratrol); PNIPAM (poly(N-isopropylacrylamide); AAM (allylamine); PPy (polypyrrole); PTX (paclitaxel); PEG (polyethylene glycol); OSA (oxidized sodium alginate); FA (folic acid); Ce6 (chlorin e6); ARS (artesunate); GNRs (gold nanorods); AGD (graphene oxide (GO)-hybridized nanogels); ICG (indocyanine green); SN (7-ethyl-10-hydroxycamptothecin (SN-38)); MS (mesoporous silica); CD47 (is an antibody); COS (chitosan oligosaccharide); DTIC (dacarbazine); v-50 (azo initiator); AuNR (gold nanorod).

3.5. Liver Cancer

By incorporating transition metals or polymer biomolecules, GBNMs can be combined to create hybrid functional materials that can greatly improve their photothermal properties [91]. For instance, Liu et al. utilized polydopamine to create a hybrid material consisting of reduced graphene oxide and mesoporous silica nanomaterial (rGO/MSNs/PDA), which was then loaded with DOX. The presence of MSNs in this system increased its drug-loading capacity, while both rGO and PDA enhanced its photothermal capacity. The results showed that rGO/MSN/PDA produced a 62.2% higher temperature postirradiation than that by GO/MSNs with the same mass concentration. The comparison tests conducted on MHCC-97L and MHCC-97H hepatocellular carcinoma cells showed that rGO/MSNs/PDA were more biocompatible than GO/MSNs in regard to in vitro cytotoxicity. On the other hand, the cell activity of MHCC97L and MHCC97H in the irradiated groups was 42.4% and 44.2% lower than that in the nonirradiated groups, indicating that photothermal therapy significantly improves the antitumor effect compared with chemotherapy alone [92]. Huang et al. conducted a study wherein they synthesized a nanohybrid by combining graphene oxide and indocyanine green modified with lactobionic acid, creating a double photothermal agent. This nanohybrid was employed in a mediated synergetic chemophotothermal therapy approach. The research revealed that as the irradiation time was prolonged, the temperature exhibited a corresponding increase. Remarkably, a photothermal conversion capability of 16.6 °C was achieved within just 5 min. In vivo assays demonstrated that this system led to an increase in temperature of 52.9 °C, which induced local hyperthermia, specifically within cancer cells. Simultaneously, the hyperthermic environment and the tumor's acidic microenvironment facilitated the release of drugs. The strategy proved to be highly effective in eradicating cancer cells and curbing tumor growth [93].

Transition metals have also been used in combination with reduced graphene oxide, generating increased photothermal conversion for this type of cancer [94]. In this work, a 980 nm laser at 1.0 W was used to irradiate a Cu₂-xSe@rGO system coated with PAH, folic acid (FA), and DOX. A temperature increase from ~25 to 55 °C was obtained after 10 min of irradiation. On the other hand, no obvious cytotoxicity was observed when the concentrations of Cu₂-xSe@rGO were lower than 75 µg/mL. The cell viability showed a significant decrease after NIR irradiation, and the inhibition ratio against HEP-2 cells increased with Cu₂-xSe@rGO-FA concentration.

3.6. Pancreatic Cancer

Eco-friendly methods for reducing GO have been investigated as an alternative to conventional methods that involve toxic chemicals. One of them is the reduction using an extract of *Salvia spinosa*. Yang et al. used the bioactive components of the extract of *Salvia spinosa* to produce rGO and evaluated its photothermal efficacy at different concentrations and power densities. The results obtained in the study showed that unmodified rGO achieved a maximum temperature increase after 4 min of laser irradiation at 808 nm with a power density of 1.7 W/cm². The treatment of the Panc02-H7 PC cell line with laser light alone did not result in significant cell death. However, after laser irradiation, the rGO-treated groups showed higher levels of cell death in comparison to GO, even after increasing the GO concentration four-fold [95]. Wu and their team utilized a traditional method of reducing GO using hydrazine. The produced rGO was modified with C18-PMH-mPEG5000, and the photothermal capacity was examined by exposing it to NIR irradiation from the second window (980 nm laser) at varying intensities. In particular, when the system was used at a concentration of 50 µg/mL and power intensity of 1.5 W/cm², it was able to reach a temperature of almost 80 °C. The results from the in vivo photothermal study, utilizing a lower laser power intensity of 0.5 W/cm² along with 2 mg/kg of modified rGO, revealed that tumors located in the center and bottom regions exhibited a temperature of approximately 68 °C. The findings of this work demonstrate that, with a higher laser wavelength, it is possible to attain deeper therapeutic temperatures [96].

Among the studies that examined GO for pancreatic cancer, Ying et al. conducted a study that employed a combination of photothermal therapy and gene therapy through modification with small interfering RNA (siRNA). The outcomes of their *in vivo* antitumor investigation demonstrated that utilizing GO-based nanoformulations in tandem with near-infrared light led to a remarkable reduction in tumor volume growth, achieving up to an 80% decrease. Notably, the synergistic effects of GO-siRNA nanoformulations and NIR-light treatment resulted in the complete remission of tumors in one-third of the experimental mice. Regarding toxicity, *in vivo* assessments indicated that GO exhibited minimal harmful effects. However, it is crucial to highlight that the intravenous administration of folic acid-GO nanoparticles resulted in rapid mortality among mice, while intraperitoneal injection showed no side effects or associated fatalities [95].

3.7. Ovarian Cancer

In an emerging treatment to improve the therapeutic efficacy against ovarian cancer, a 1,061 nm diode laser (spot size: 1 cm) with different power densities was used. The temperature of the hybrid between gold nanoparticles coated with reduced graphene oxide (rGO-AuNPs) was approximately 61 °C, which was higher than that of AuNPs (15 °C) and rGO (33 °C). The rGO-AuNPs enabled high tumor accumulation post-intravenous-injection into SKOV-3 tumor-bearing mice, resulting in an intensive photoacoustic (PA) signal. More importantly, the PA signal was observed only in the tumor tissue, and no background signal was present in the skin, indicating the higher contrast and resolution of the NIR-II PA imaging of the rGO-AuNP compared with conventional NIR-I PA imaging. Finally, compared to the continued tumor growth in other control groups, the tumors in mice treated with the rGO-AuNP postcombinatorial treatment with PA and PTT were effectively eliminated without recurrence [97].

3.8. Tongue Squamous Cancer

Hao et al. utilized tea polyphenol to reduce and functionalize GO (TPG). Then, a new and versatile anti-PDL1-conjugated TPG (TPDL1) loaded with DOX was developed. Cell-death-ligand 1 (PDL1) is a specifically expressed cell membrane antigen that shows high expression in cancer cells and low expression in normal cells. The reduced version of GO presented high photothermal conversion efficiency, reaching 60 °C after 9 min of irradiation. Additionally, after three repeated cycles of irradiation for 3 min followed by cooling for 3 min, the system showed reversible photothermal stability. The release of DOX from TPDL1 was pH-dependent, and at pH 5.0 and 48 h, it reached 22.60% release. However, the photothermal effect increased the DOX release percentage from 13.26% (−NIR) to 45.30% (+NIR) at pH 5.0 for only 6 h [98]. A similar photothermal response was obtained in a system based on rGO modified with bovine serum albumin used as a carrier nanoplatform for zeolitic imidazolate framework-8 (BSArGO@ZIF-8) for combinatorial ion interference (IIT) and PTT (Figure 7A(a)). The system serves as an efficient Zn²⁺ source that can disrupt intracellular homeostasis, causing an increase in the level of reactive oxygen species (ROS), mitochondrial damage, and cell apoptosis. The authors state that GO should be reduced to increase the photothermal effect. In this study, the cell viability of SCC25 cells after BSArGO@ZIF-8 NSs and NIR irradiation decreased to ~15% (Figure 7B(a)). Similarly, the viability of Cal27 cells was approximately ~20% after irradiation (Figure 7B(b)). However, NIR irradiation alone at 808 nm (1 W/cm²) for 10 min had negligible effects on Cal27 cells. Furthermore, live/dead staining of Cal27 cells was performed. Figure 7B(d)) shows that many dead cells were imaged after BSArGO@ZIF-8 NSs treatment compared with the control group (Figure 7B(c)). After NIR irradiation (Figure 7B(e)), more dead cells emerged, and few live cells could be observed [99].

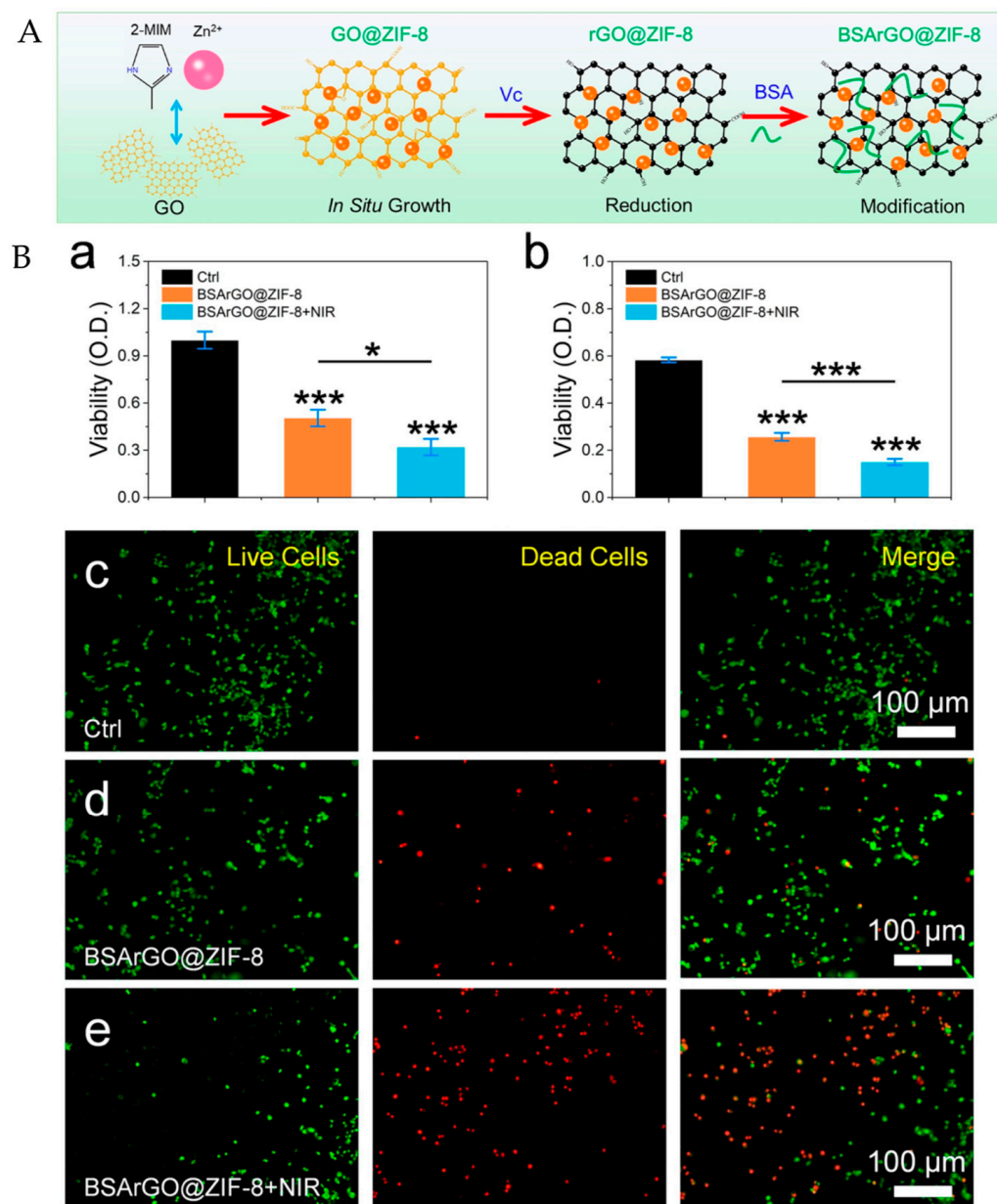


Figure 7. (A) Schematic preparation of BSArGO@ZIF-8 NSs. (B) Synergistic effect of PTT and IIT. (a,b) Viability of SCC25 cells and Cal27 cells after BSArGO@ZIF-8 NSs treatment with or without NIR irradiation, respectively (* $p < 0.05$, *** $p < 0.001$). (c–e) Live/dead staining of Cal27 cells treated with BSArGO@ZIF-8 NSs with or without NIR irradiation. Adapted from [99] Copyright 2022, American Chemical Society.

3.9. Hybrid Magnetic Graphene-Based Nanomaterials

Magnetic nanoparticles (MNPs) [30,100], including magnetite (Fe_3O_4) and maghemite (Fe_2O_3), can be magnetically controlled by an external magnetic field, making them valuable for medical applications [101–103]. In this sense, Dash et al. developed a hybrid between rGO and magnetic nanoparticles (mrGO) loaded with DOX (mgGOG) that exhibited excellent magnetic and photothermal properties for targeted drug delivery and PTT. The SQUID analysis confirmed the superparamagnetic properties of all the samples, with remanent magnetizations of 0.14, 0.04, and 0.03 emu/g for CMNPs (citrate-coated magnetic nanoparticles), mrGO, and mrGOG, respectively. The photothermal results obtained using an 808 nm NIR laser (1.5 W/cm^2) showed that mrGO possesses a higher photothermal response than rGO, reaching 60°C at 150 s. This temperature supports

previous findings that iron oxide nanoparticles have a photothermal response after NIR irradiation [104]. Guided drug delivery was confirmed by incubating mrGOG with U87 cells under the guidance of a magnet glued to the bottom of the well surface. The results obtained from the live/dead cell viability staining assay revealed that dead cells, marked by red fluorescence, accumulated in the magnetically targeted zone at which mrGOG/DOX was attracted and concentrated, causing cell death. However, the density of dead cells was lower than expected due to their detachment from the well surface after cell death. On the other hand, live cells, identified by green fluorescence, were mainly located outside the targeted zone and lacked magnetic guidance. This suggests that an external magnetic field could guide mrGOG/DOX to the tumor site, increasing the drug concentration and offering the potential for dual-targeted anticancer therapy in vivo [105]. Ardakani et al. used two different concentrations of reduced graphene oxide to increase the therapeutic efficiency of Fe₃O₄@Au nanoparticles in the in vitro photothermal radiotherapy of KB oral squamous carcinoma. The photothermal conversion efficiency results showed that Fe₃O₄@Au/rGO nanostructures (NSs) under 808 nm laser irradiation and 1.8 W/cm² had a high photothermal conversion efficiency (61%) and were very suitable for photothermal applications. Viability assays showed that using NSs+PPT is approximately 13 times more effective than using the control group (without NIR) [106]. Another hybrid between magnetite and rGO without other modification was prepared to investigate the photothermal capacity at two concentrations (50 and 100 µg/mL), irradiating them with an 804 nm optical laser at 1 W/cm² for 5 min. A similar increase in the temperature was observed for both concentrations. The authors suggest that this could be associated with the insoluble nature of the hybrid or the incomplete reduction of GO that also influences the lower temperature reached. In vitro results showed that photothermal therapy with the hybrid reduced cell viability to 32.6% and 23.7% at 50 and 100 µg/mL, respectively, while untreated cells were not noticeably affected; even under laser exposure, viability was maintained at over 83% [107]. Soysal et al. prepared the same hybrid between magnetite and rGO but modified it with polyaniline (S-rGO-Fe₃O₄-PANI), with excellent photothermal performance. The maximum temperature achieved after 10 min of long irradiation at 808 nm and 3.0 W/cm² was ~60 °C. At a laser power density of 2.0 W/cm² and a concentration of 100 µg mL⁻¹, the temperature of the nanocomposite increased by 56.7 °C in comparison to deionized water, and an 86.3% photothermal conversion efficiency was obtained [108].

Du et al. used rGO to anchor iron oxide, polyethyleneimine (PEI), and indocyanine green (RGI_{1.8k}-ICG) as a drug model. The hybrid did not exhibit significant cytotoxicity and showed good biocompatibility. The level of cell destruction varied with different laser densities; for example, at laser densities lower than 0.3 W/cm², no cell destruction effects were observed for the PBS, ICG, RGI_{1.8k}, and RGI_{1.8k}-ICG groups. However, it decreased rapidly for the RGI_{1.8k}-ICG group when the laser density reached 0.5 W/cm² and for the RGI_{1.8k} group when it reached 0.7 W/cm². The in vivo results obtained using a laser density of 0.3 W/cm² produced a temperature at the tumor site of approximately 55 °C, which was sufficient to ablate the cancer cells efficiently and cause the near disappearance of the tumor. However, without laser irradiation, the tumor grew rapidly and became almost as large as that of the negative control group after 15 days [109].

The photothermal effect of GO functionalized with Fe₃O₄ (MG-NH₂-PEG) and DOX was also evaluated in the treatment of breast cancer. A rapid increase in the temperature pursuant to a concentration-dependent behavior was obtained when an 808 nm NIR laser was used with a power density of 1 W/cm². The MCF-7 cell line was incubated with MG-NH₂-PEG for 2 h and irradiated for 5 min with varying power densities. Then, in vitro cytotoxicity tests were performed, showing that the cells were killed after laser irradiation. The untreated cells maintained their viability despite the higher laser irradiation (up to 2 W/cm²). Furthermore, the cells treated with 20 min of NIR laser irradiation closer to the magnetic field were significantly destroyed, while those located at a further distance remained largely unaffected [110].

Gong et al. prepared a novel multifunctional hybrid material, which is depicted in Figure 8A. The MGO-TCA-FA hybrid synthesis process involves modifying magnetic graphene oxide (MGO) with trimethyl cholic acid (TCA) and folic acid (FA) simultaneously. The hydrophobic anticancer drug DOX was then successfully loaded onto the modified MGO to create MGO-TCA-FA@DOX nanocomposites. This hybrid was effective in providing chemotherapy and photothermal therapy for liver cancer. Figure 8B(a) shows that when exposed to 808 nm and 2 W/cm^2 for 5 min, the solution temperature increased from $21 \text{ }^\circ\text{C}$ to $60 \text{ }^\circ\text{C}$ with the concentration from 0 mg/mL to 1.0 mg/mL . Figure 8B(b) shows the respective thermal images obtained. In addition, MGO-TCA-FA also exhibited laser power intensity dependency (Figure 8B(c)), and, more importantly, it had good photothermal stability after four 20 min laser on/off cycles (Figure 8B(d)) [111].

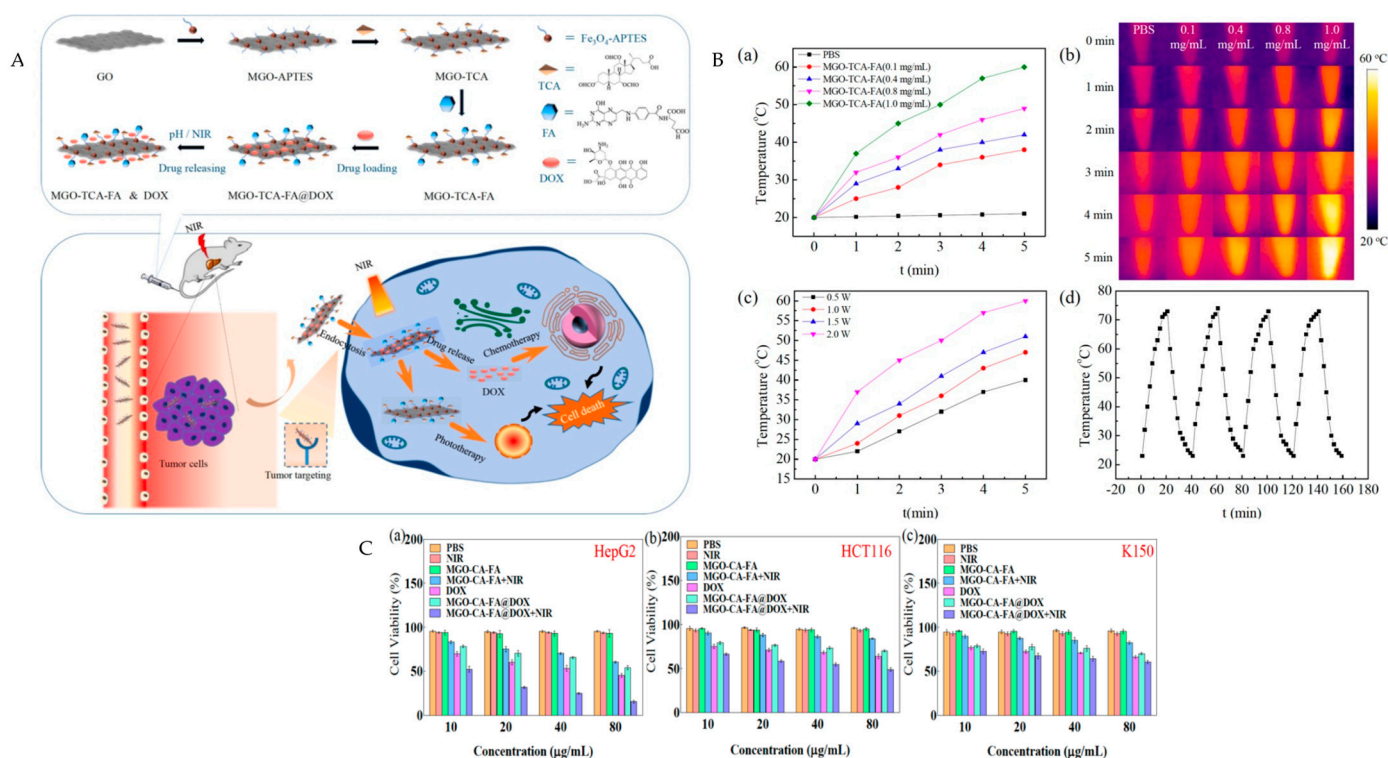


Figure 8. (A) Schematic diagram of MGO-TCA-FA@DOX and its photochemotherapy effect on cancer cells. (B) Temperature-change curves (a) and corresponding infrared thermal images (b) of MGO-TCA-FA solutions at different concentrations obtained by using the thermal imaging system; (c) temperature-rise curve of MGO-TCA-FA irradiated with different laser irradiation intensities (808 nm); (d) temperature-variation curve of MGO-TCA-FA with 20 min laser on/off cycles. (C) Cell survival rate of HepG2 (a), HCT-116 (b), and K150 (c) cells treated with PBS, PBS + NIR, MGO-TCA-FA, MGO-TCA-FA + NIR, DOX, MGO-TCA-FA@DOX, and MGO-TCA-FA@DOX + NIR. The concentrations of MGO-TCA-FA and MGO-TCA-FA@DOX were 10 , 20 , 40 , and $80 \mu\text{g mL}^{-1}$, respectively. Adapted from [111] Copyright 2021, Elsevier Inc.

4. Challenges and Perspectives

Methods to utilize graphene nanomaterials in biomedical applications have advanced significantly in recent years. GO and rGO have been identified as potential photothermal agents in nanomedicine due to their physicochemical properties and high biocompatibility. However, there are still several issues that need to be addressed before photothermal therapy based on these nanomaterials is implemented in clinical trials, especially when tumors are located deep within tissues or when metastasis is spread throughout the body.

First, many studies reviewed here have focused on using laser light from the NIR-I window (mostly 808 nm) to induce hyperthermia. Although this wavelength is attractive

because biological systems lack chromophores that absorb in this region, thus reducing scattering and autofluorescence, it is not very effective in treating tumors that are deep or sizable because its penetration depth in body tissues is limited. This issue is particularly important in clinical settings because if the method is combined with GO as PTA, photothermal therapy will be inefficient. For that reason, the NIR-II window is a better option because it can penetrate deeper into tissues due to less scattering with longer wavelengths. Additionally, higher power intensities can be used since longer wavelengths have less energy per photon [6,10,14,48,77]. Therefore, when designing new strategies to treat cancer photothermally using GBNMs, researchers should consider the NIR-II region for irradiation.

Another critical issue to consider when designing clinical trials is the potential harm caused by GBNMs, modified GBNMs, and NIR irradiation to human health. The toxicity of GBNMs can be influenced by a range of factors, including their size, chemical composition, surface charge, and aggregation state [13]. Although GO and rGO have exhibited strong biocompatibility in various studies, it is important to note that their toxicity might escalate due to successive functionalization. Consequently, a prudent recommendation is to prioritize the utilization of biomimetic molecules, particularly those that have received FDA approval, for any forthcoming therapeutic strategies involving GBNMs. This emphasis is even more significant when GBNMs are modified for multimodal detection and treatment or for addressing cancer through combinatorial techniques [112].

In the upcoming years, it will be crucial to conduct additional research that involves the utilization of FDA-approved modified rGO, the application of NIR-II light sources for irradiation, the incorporation of 3D tumor models for *in vitro* assays, and the assessment of *in vivo* toxicity. This collective effort will play a pivotal role in advancing the transition from laboratory testing to eventual clinical applications.

5. Conclusions

Graphene oxide and reduced graphene oxide function as unique photothermal agents due to their remarkable structural features. While the materials exhibit comparable structures, their photothermal capacities are very different, affecting the success of photothermal therapy for cancer treatment.

For GO, high concentrations and laser power intensities were necessary to generate the photothermal effect. However, in most cases, the temperature did not surpass 50 °C. Instead, the development of hybrids involving GO and other photothermal materials and anticancer drugs displayed better photothermal effects with similar therapeutic results to those obtained for rGO.

Compared with GO, rGO achieved greater photothermal conversion under the same NIR irradiation conditions. Moreover, a significant decrease in the cell viability of different cancer cell lines treated was found when rGO was used as the PTA. Notably, the chemical reduction method is frequently employed for manufacturing rGO with photothermal characteristics. However, it remains uncertain whether alternative reduction methods could lead to even more substantial NIR absorption and a heightened photothermal effect.

All the GO and rGO-based systems reviewed demonstrated that the heat generated was concentration- and laser-power-intensity dependent. In addition, the use of combined PTT with a secondary therapeutic strategy showed improved therapeutic efficacy compared with that of PTT alone.

Nevertheless, most of the studies reviewed focused on the use of laser light from the NIR-I window, although the NIR-II window offers major benefits, such as a higher penetration depth and the possibility of operating at higher power intensities for irradiation. This aspect should be considered when designing and developing new photothermal strategies and looking for their potential translation to clinical use.

On the other hand, MNPs could be utilized as a guide to a specific location as well as in the photothermal response. Through MNPs, GBNMs could be modified to load drug

molecules, making them suitable for drug delivery. The use of MNPs will continue to benefit GBNM for synergistic photothermal therapy.

We hope this review can provide new insights for the future design of GBNM nanoplat-forms, especially as photothermal agents in the photothermal treatment of cancer.

Funding: This research was funded by ANID-FONDECYT 11200416, ANID-FOVI 220173 and CONICYT-FONDAP No 15130011.

Institutional Review Board Statement: Not applicable.

Informed Consent Statement: Not applicable.

Data Availability Statement: Not applicable.

Conflicts of Interest: The author declares no conflict of interest.

References

1. Sung, H.; Ferlay, J.; Siegel, R.L.; Laversanne, M.; Soerjomataram, I.; Jemal, A.; Bray, F. Global cancer statistics 2020: GLOBOCAN estimates of incidence and mortality worldwide for 36 cancers in 185 countries. *CA. Cancer J. Clin.* **2021**, *71*, 209–249. [[CrossRef](#)] [[PubMed](#)]
2. Miller, K.D.; Nogueira, L.; Devasia, T.; Mariotto, A.B.; Yabroff, K.R.; Jemal, A.; Kramer, J.; Siegel, R.L. Cancer treatment and survivorship statistics, 2022. *CA. Cancer J. Clin.* **2022**, *72*, 409–436. [[CrossRef](#)] [[PubMed](#)]
3. Thapa, R.K.; Youn, Y.S.; Jeong, J.-H.; Choi, H.-G.; Yong, C.S.; Kim, J.O. Graphene oxide-wrapped PEGylated liquid crystalline nanoparticles for effective chemo-photothermal therapy of metastatic prostate cancer cells. *Colloids Surf. B Biointerfaces* **2016**, *143*, 271–277. [[CrossRef](#)] [[PubMed](#)]
4. Chen, J.; He, G.M.; Xian, G.Y.; Su, X.Q.; Yu, L.L.; Yao, F. Mechanistic biosynthesis of SN-38 coated reduced graphene oxide sheets for photothermal treatment and care of patients with gastric cancer. *J. Photochem. Photobiol. B Biol.* **2020**, *204*, 111736. [[CrossRef](#)]
5. Dong, H.; Jin, M.; Liu, Z.; Xiong, H.; Qiu, X.; Zhang, W.; Guo, Z. In vitro and in vivo brain-targeting chemo-photothermal therapy using graphene oxide conjugated with transferrin for Gliomas. *Lasers Med. Sci.* **2016**, *31*, 1123–1131. [[CrossRef](#)]
6. Zhang, L.; Oudeng, G.; Wen, F.; Liao, G. Recent advances in near-infrared-II hollow nanoplat-forms for photothermal-based cancer treatment. *Biomater. Res.* **2022**, *26*, 61. [[CrossRef](#)]
7. Doughty, A.C.V.; Hoover, A.R.; Layton, E.; Murray, C.K.; Howard, E.W.; Chen, W.R. Nanomaterial applications in photothermal therapy for cancer. *Materials* **2019**, *12*, 779. [[CrossRef](#)]
8. Ren, Y.; Yan, Y.; Qi, H. Photothermal conversion and transfer in photothermal therapy: From macroscale to nanoscale. *Adv. Colloid Interface Sci.* **2022**, *308*, 102753. [[CrossRef](#)]
9. Han, H.S.; Choi, K.Y. Advances in nanomaterial-mediated photothermal cancer therapies: Toward clinical applications. *Biomedicines* **2021**, *9*, 305. [[CrossRef](#)]
10. Liu, P.; Ye, M.; Wu, Y.; Wu, L.; Lan, K.; Wu, Z. Hyperthermia combined with immune checkpoint inhibitor therapy: Synergistic sensitization and clinical outcomes. *Cancer Med.* **2023**, *12*, 3201–3221. [[CrossRef](#)]
11. Jing, Z.; Du, Q.; Zhang, X.; Zhang, Y. Nanomedicines and nanomaterials for cancer therapy: Progress, challenge and perspectives. *Chem. Eng. J.* **2022**, *446*, 137147. [[CrossRef](#)]
12. Giri, P.M.; Banerjee, A.; Layek, B. A Recent Review on Cancer Nanomedicine. *Cancers* **2023**, *15*, 2256. [[CrossRef](#)] [[PubMed](#)]
13. Karthikeyan, L.; Sobhana, S.; Yasothamani, V.; Gowsalya, K.; Vivek, R. Multifunctional theranostic nanomedicines for cancer treatment: Recent progress and challenges. *Biomed. Eng. Adv.* **2023**, *5*, 100082. [[CrossRef](#)]
14. Xu, C.; Pu, K. Second near-infrared photothermal materials for combinational nanotheranostics. *Chem. Soc. Rev.* **2021**, *50*, 1111–1137. [[CrossRef](#)]
15. Wei, W.; Zhang, X.; Zhang, S.; Wei, G.; Su, Z. Biomedical and bioactive engineered nanomaterials for targeted tumor photothermal therapy: A review. *Mater. Sci. Eng. C* **2019**, *104*, 109891. [[CrossRef](#)]
16. Gao, S.; Yang, X.; Xu, J.; Qiu, N.; Zhai, G. Nanotechnology for Boosting Cancer Immunotherapy and Remodeling Tumor Microenvironment: The Horizons in Cancer Treatment. *ACS Nano* **2021**, *15*, 12567–12603. [[CrossRef](#)]
17. Saneja, A.; Kumar, R.; Arora, D.; Kumar, S.; Panda, A.K.; Jaglan, S. Recent advances in near-infrared light-responsive nanocarriers for cancer therapy. *Drug Discov. Today* **2018**, *23*, 1115–1125. [[CrossRef](#)]
18. Shukla, A.; Maiti, P. Nanomedicine and versatile therapies for cancer treatment. *MedComm* **2022**, *3*, e163. [[CrossRef](#)]
19. Yang, F.; He, Q.; Dai, X.; Zhang, X.; Song, D. The potential role of nanomedicine in the treatment of breast cancer to overcome the obstacles of current therapies. *Front. Pharmacol.* **2023**, *14*, 1–12. [[CrossRef](#)]
20. Gupta, N.; Malviya, R. Understanding and advancement in gold nanoparticle targeted photothermal therapy of cancer. *Biochim. Biophys. Acta Rev. Cancer* **2021**, *1875*, 188532. [[CrossRef](#)]
21. Sheikhpour, M.; Golbabaie, A.; Kasaiean, A. Carbon nanotubes: A review of novel strategies for cancer diagnosis and treatment. *Mater. Sci. Eng. C* **2017**, *76*, 1289–1304. [[CrossRef](#)]
22. Eldridge, B.N.; Bernish, B.W.; Fahrenholtz, C.D.; Singh, R. Photothermal Therapy of Glioblastoma Multiforme Using Multiwalled Carbon Nanotubes Optimized for Diffusion in Extracellular Space. *ACS Biomater. Sci. Eng.* **2016**, *2*, 963–976. [[CrossRef](#)] [[PubMed](#)]
23. Liu, J.; Dong, J.; Zhang, T.; Peng, Q. Graphene-based nanomaterials and their potentials in advanced drug delivery and cancer therapy. *J. Control Release* **2018**, *286*, 64–73. [[CrossRef](#)]

24. Zhang, Y.; Zhang, S.; Zhang, Z.; Ji, L.; Zhang, J.; Wang, Q.; Guo, T.; Ni, S.; Cai, R.; Mu, X.; et al. Recent Progress on NIR-II Photothermal Therapy. *Front. Chem.* **2021**, *9*, 1–26. [[CrossRef](#)] [[PubMed](#)]
25. Ito, A.M.; Vemula, S.L.; Gupta, M.T.; Giram, M.V.; Kumar, S.A.; Ghosh, B.; Biswas, S. Multifunctional graphene oxide nanoparticles for drug delivery in cancer. *J. Control Release Off. J. Control Release Soc.* **2022**, *350*, 26–59. [[CrossRef](#)]
26. Taheriazam, A.; Abad, G.G.Y.; Hajimazdarany, S.; Imani, M.H.; Ziaolhagh, S.; Zandieh, M.A.; Bayanzadeh, S.D.; Mirzaei, S.; Hamblin, M.R.; Entezari, M.; et al. Graphene oxide nanoarchitectures in cancer biology: Nano-modulators of autophagy and apoptosis. *J. Control Release* **2023**, *354*, 503–522. [[CrossRef](#)]
27. Qi, K.; Sun, B.; Liu, S.; Zhang, M. Research progress on carbon materials in tumor photothermal therapy. *Biomed. Pharmacother.* **2023**, *165*, 115070. [[CrossRef](#)]
28. Wang, Y.; Li, J.; Li, X.; Shi, J.; Jiang, Z.; Zhang, C.Y. Graphene-based nanomaterials for cancer therapy and anti-infections. *Bioact. Mater.* **2022**, *14*, 335–349. [[CrossRef](#)] [[PubMed](#)]
29. Cui, G.; Wu, J.; Lin, J.; Liu, W.; Chen, P.; Yu, M.; Zhou, D.; Yao, G. Graphene-based nanomaterials for breast cancer treatment: Promising therapeutic strategies. *J. Nanobiotechnol.* **2021**, *19*, 211. [[CrossRef](#)]
30. Farzin, A.; Etesami, S.A.; Quint, J.; Memic, A.; Tamayol, A. Magnetic Nanoparticles in Cancer Therapy and Diagnosis. *Adv. Healthc. Mater.* **2020**, *9*, 1901058. [[CrossRef](#)]
31. Cheon, Y.A.; Bae, J.H.; Chung, B.G. Reduced Graphene Oxide Nanosheet for Chemo-photothermal Therapy. *Langmuir* **2016**, *32*, 2731–2736. [[CrossRef](#)]
32. Maiti, D.; Tong, X.; Mou, X.; Yang, K. Carbon-Based Nanomaterials for Biomedical Applications: A Recent Study. *Front. Pharmacol.* **2019**, *9*, 1–16. [[CrossRef](#)]
33. Tarcan, R.; Todor-Boer, O.; Petrovai, I.; Leordean, C.; Astilean, S.; Botiz, I. Reduced graphene oxide today. *J. Mater. Chem. C* **2020**, *8*, 1198–1224. [[CrossRef](#)]
34. Novoselov, K.S.; Geim, A.K.; Morozov, S.V.; Jiang, D.; Zhang, Y.; Dubonos, S.V.; Grigorieva, I.V.; Firsov, A.A. Electric field in atomically thin carbon films. *Science* **2004**, *306*, 666–669. [[CrossRef](#)] [[PubMed](#)]
35. Hummers, W.S.; Offeman, R.E. Preparation of Graphitic Oxide. *J. Am. Chem. Soc.* **1958**, *80*, 1339.
36. Dreyer, D.R.; Park, S.; Bielawski, C.W.; Ruoff, R.S. The chemistry of graphene oxide. *Chem. Soc. Rev.* **2010**, *39*, 228–240. [[CrossRef](#)]
37. Agarwal, V.; Zetterlund, P.B. Strategies for reduction of graphene oxide—A comprehensive review. *Chem. Eng. J.* **2021**, *405*, 127018. [[CrossRef](#)]
38. Morales-Narváez, E.; Baptista-Pires, L.; Zamora-Gálvez, A.; Merkoçi, A. Graphene-Based Biosensors: Going Simple. *Adv. Mater.* **2017**, *29*, 1604905. [[CrossRef](#)]
39. De Melo-Diogo, D.; Lima-Sousa, R.; Alves, C.G.; Costa, E.C.; Louro, R.O.; Correia, I.J. Functionalization of graphene family nanomaterials for application in cancer therapy. *Colloids Surf. B Biointerfaces* **2018**, *171*, 260–275. [[PubMed](#)]
40. Loh, K.P.; Bao, Q.; Eda, G.; Chhowalla, M. Graphene oxide as a chemically tunable platform for optical applications. *Nat. Chem.* **2010**, *2*, 1015–1024. [[CrossRef](#)]
41. Rathnayake, R.M.N.M.; Wijayasinghe, H.W.M.A.C.; Pitawala, H.M.T.G.A.; Yoshimura, M.; Huang, H.-H. Synthesis of graphene oxide and reduced graphene oxide by needle plating natural vein graphite. *Appl. Surf. Sci.* **2017**, *393*, 309–315. [[CrossRef](#)]
42. Ossonon, B.D.; Bélanger, D. Synthesis and characterization of sulfophenyl-functionalized reduced graphene oxide sheets. *RSC Adv.* **2017**, *7*, 27224–27234. [[CrossRef](#)]
43. Li, Y.; Yuan, S.; Xia, Y.; Zhao, W.; Easton, C.D.; Selomulya, C.; Zhang, X. Mild annealing reduced graphene oxide membrane for nanofiltration. *J. Memb. Sci.* **2020**, *601*, 117900. [[CrossRef](#)]
44. Jin, Y.; Zheng, Y.; Podkolzin, S.G.; Lee, W. Band gap of reduced graphene oxide tuned by controlling functional groups. *J. Mater. Chem. C* **2020**, *8*, 4885–4894. [[CrossRef](#)]
45. Báez, D.; Pardo, H.; Laborda, I.; Marco, J.; Yáñez, C.; Bollo, S. Reduced Graphene Oxides: Influence of the Reduction Method on the Electrocatalytic Effect towards Nucleic Acid Oxidation. *Nanomaterials* **2017**, *7*, 168. [[CrossRef](#)] [[PubMed](#)]
46. Mei, X.; Meng, X.; Wu, F. Hydrothermal method for the production of reduced graphene oxide. *Phys. E Low-Dimens. Syst. Nanostruct.* **2015**, *68*, 81–86. [[CrossRef](#)]
47. Robinson, J.T.; Tabakman, S.M.; Liang, Y.; Wang, H.; Sanchez Casalongue, H.; Vinh, D.; Dai, H. Ultrasmall Reduced Graphene Oxide with High Near-Infrared Absorbance for Photothermal Therapy. *J. Am. Chem. Soc.* **2011**, *133*, 6825–6831. [[CrossRef](#)] [[PubMed](#)]
48. Yu, Z.; Chan, W.K.; Zhang, Y.; Tan, T.T.Y. Near-infrared-II activated inorganic photothermal nanomedicines. *Biomaterials* **2021**, *269*, 120459. [[CrossRef](#)]
49. Sun, J.; Zhao, H.; Xu, W.; Jiang, G.Q. Recent advances in photothermal therapy-based multifunctional nanoplatfoms for breast cancer. *Front. Chem.* **2022**, *10*, 1–7. [[CrossRef](#)]
50. Zhang, W.; Guo, Z.; Huang, D.; Liu, Z.; Guo, X.; Zhong, H. Synergistic effect of chemo-photothermal therapy using PEGylated graphene oxide. *Biomaterials* **2011**, *32*, 8555–8561. [[CrossRef](#)]
51. Zhu, X.; Zhang, Y.; Huang, H.; Zhang, H.; Hou, L.; Zhang, Z. Functionalized graphene oxide-based thermosensitive hydrogel for near-infrared chemo-photothermal therapy on tumor. *J. Biomater. Appl.* **2016**, *30*, 1230–1241. [[CrossRef](#)] [[PubMed](#)]
52. Sahu, A.; Choi, W.I.; Lee, J.H.; Tae, G. Graphene oxide mediated delivery of methylene blue for combined photodynamic and photothermal therapy. *Biomaterials* **2013**, *34*, 6239–6248. [[CrossRef](#)] [[PubMed](#)]
53. De Melo-Diogo, D.; Pais-Silva, C.; Dias, D.R.; Moreira, A.F.; Correia, I.J. Strategies to Improve Cancer Photothermal Therapy Mediated by Nanomaterials. *Adv. Healthc. Mater.* **2017**, *6*, 1700073. [[CrossRef](#)]

54. Chien, Y.-H.; Chan, K.K.; Anderson, T.; Kong, K.V.; Ng, B.K.; Yong, K.-T. Advanced Near-Infrared Light-Responsive Nanomaterials as Therapeutic Platforms for Cancer Therapy. *Adv. Ther.* **2019**, *2*, 1800090. [[CrossRef](#)]
55. Yang, K.; Wan, J.; Zhang, S.; Tian, B.; Zhang, Y.; Liu, Z. The influence of surface chemistry and size of nanoscale graphene oxide on photothermal therapy of cancer using ultra-low laser power. *Biomaterials* **2012**, *33*, 2206–2214. [[CrossRef](#)]
56. Hashemi, M.; Omidi, M.; Muralidharan, B.; Smyth, H.; Mohagheghi, M.A.; Mohammadi, J.; Milner, T.E. Evaluation of the Photothermal Properties of a Reduced Graphene Oxide/Arginine Nanostructure for Near-Infrared Absorption. *ACS Appl. Mater. Interfaces* **2017**, *9*, 32607–32620. [[CrossRef](#)] [[PubMed](#)]
57. Li, X.; Wang, Y.; Liu, T.; Zhang, Y.; Wang, C.; Xie, B. Ultrasmall graphene oxide for combination of enhanced chemotherapy and photothermal therapy of breast cancer. *Colloids Surf. B Biointerfaces* **2023**, *225*, 113288. [[CrossRef](#)] [[PubMed](#)]
58. Dheyab, M.A.; Aziz, A.A.; Khaniabadi, P.M.; Jameel, M.S.; Oladzadabbasabadi, N.; Rahman, A.A.; Braim, F.S.; Mehrdel, B. Gold nanoparticles-based photothermal therapy for breast cancer. *Photodiagnosis Photodyn. Ther.* **2023**, *42*, 103312. [[CrossRef](#)] [[PubMed](#)]
59. Wang, X.; Han, Q.; Yu, N.; Li, J.; Yang, L.; Yang, R.; Wang, C. Aptamer-conjugated graphene oxide-gold nanocomposites for targeted chemo-photothermal therapy of cancer cells. *J. Mater. Chem. B* **2015**, *3*, 4036–4042. [[CrossRef](#)]
60. Roy, S.; Sarkar, A.; Jaiswal, A. Poly(allylamine hydrochloride)-functionalized reduced graphene oxide for synergistic chemo-photothermal therapy. *Nanomedicine* **2019**, *14*, 255–274. [[CrossRef](#)]
61. Lima-Sousa, R.; Alves, C.G.; Melo, B.L.; Moreira, A.F.; Mendonça, A.G.; Correia, I.J.; de Melo-Diogo, D. Poly(2-ethyl-2-oxazoline) functionalized reduced graphene oxide: Optimization of the reduction process using dopamine and application in cancer photothermal therapy. *Mater. Sci. Eng. C* **2021**, *130*, 112468. [[CrossRef](#)] [[PubMed](#)]
62. Du, P.; Yan, J.; Long, S.; Xiong, H.; Wen, N.; Cai, S.; Wang, Y.; Peng, D.; Liu, Z.; Liu, Y. Tumor microenvironment and NIR laser dual-responsive release of berberine 9- O -pyrazole alkyl derivative loaded in graphene oxide nanosheets for chemo-photothermal synergetic cancer therapy. *J. Mater. Chem. B* **2020**, *8*, 4046–4055. [[CrossRef](#)] [[PubMed](#)]
63. Wang, C.; Wang, X.; Chen, Y.; Fang, Z. In-vitro photothermal therapy using plant extract polyphenols functionalized graphene sheets for treatment of lung cancer. *J. Photochem. Photobiol. B Biol.* **2020**, *204*, 111587. [[CrossRef](#)] [[PubMed](#)]
64. Liu, X.; Wu, X.; Xing, Y.; Zhang, Y.; Zhang, X.; Pu, Q.; Wu, M.; Zhao, J.X. Reduced Graphene Oxide/Mesoporous Silica Nanocarriers for pH-Triggered Drug Release and Photothermal Therapy. *ACS Appl. Bio Mater.* **2020**, *3*, 2577–2587. [[CrossRef](#)] [[PubMed](#)]
65. Zhou, A.; Bai, J.; Hong, W.; Bai, H. Electrochemically reduced graphene oxide: Preparation, composites, and applications. *Carbon N. Y.* **2022**, *191*, 301–332. [[CrossRef](#)]
66. Akhavan, O.; Ghaderi, E. Graphene nanomesh promises extremely efficient in vivo photothermal therapy. *Small* **2013**, *9*, 3593–3601. [[CrossRef](#)]
67. Zhang, Y.; Zhang, H.; Wang, Y.; Wu, H.; Zeng, B.; Zhang, Y.; Tian, Q.; Yang, S. Hydrophilic graphene oxide/bismuth selenide nanocomposites for CT imaging, photoacoustic imaging, and photothermal therapy. *J. Mater. Chem. B* **2017**, *5*, 1846–1855. [[CrossRef](#)]
68. Zhang, H.; Wu, H.; Wang, J.; Yang, Y.; Wu, D.; Zhang, Y.; Zhang, Y.; Zhou, Z.; Yang, S. Graphene oxide-BaGdF₅ nanocomposites for multi-modal imaging and photothermal therapy. *Biomaterials* **2015**, *42*, 66–77. [[CrossRef](#)]
69. SreeHarsha, N.; Maheshwari, R.; Al-Dhubiab, B.E.; Tekade, M.; Sharma, M.C.; Venugopala, K.N.; Tekade, R.K.; Alzahrani, A.M. Graphene-based hybrid nanoparticle of doxorubicin for cancer chemotherapy. *Int. J. Nanomed.* **2019**, *14*, 7419–7429. [[CrossRef](#)]
70. Qiang, L.; Cai, Z.; Jiang, W.; Liu, J.; Tai, Z.; Li, G.; Gong, C.; Gao, S.; Gao, Y. A novel macrophage-mediated biomimetic delivery system with NIR-triggered release for prostate cancer therapy. *J. Nanobiotechnol.* **2019**, *17*, 83. [[CrossRef](#)]
71. Khan, M.S.; Pandey, S.; Bhaisare, M.L.; Gedda, G.; Talib, A.; Wu, H.-F. Graphene oxide@gold nanorods for chemo-photothermal treatment and controlled release of doxorubicin in mice Tumor. *Colloids Surf. B Biointerfaces* **2017**, *160*, 543–552. [[CrossRef](#)]
72. Kumawat, M.K.; Thakur, M.; Bahadur, R.; Kaku, T.; Prabhuraj, R.S.; Suchitta, A.; Srivastava, R. Preparation of graphene oxide-graphene quantum dots hybrid and its application in cancer theranostics. *Mater. Sci. Eng. C* **2019**, *103*, 109774. [[CrossRef](#)]
73. Pang, Y.; Mai, Z.; Wang, B.; Wang, L.; Wu, L.; Wang, X.; Chen, T. Artesunate-modified nano-graphene oxide for chemo-photothermal cancer therapy. *Oncotarget* **2017**, *8*, 93800–93812. [[CrossRef](#)]
74. Xu, X.; Wang, J.; Wang, Y.; Zhao, L.; Li, Y.; Liu, C. Formation of graphene oxide-hybridized nanogels for combinative anticancer therapy. *Nanomed. Nanotechnol. Biol. Med.* **2018**, *14*, 2387–2395. [[CrossRef](#)]
75. Guo, S.; Song, Z.; Ji, D.K.; Reina, G.; Fauny, J.D.; Nishina, Y.; Ménard-Moyon, C.; Bianco, A. Combined Photothermal and Photodynamic Therapy for Cancer Treatment Using a Multifunctional Graphene Oxide. *Pharmaceutics* **2022**, *14*, 1365. [[CrossRef](#)]
76. Peng, Z.; Chang, Q.; Xing, M.; Lu, F. Active Hydrophilic Graphene Oxide Nanocomposites Delivery Mediated by Adipose-Derived Stem Cell for Elevated Photothermal Therapy of Breast Cancer. *Int. J. Nanomed.* **2023**, *18*, 971–986. [[CrossRef](#)]
77. Kang, W.; Liu, Y.; Wang, W. Light-responsive nanomedicine for cancer immunotherapy. *Acta Pharm. Sin. B* **2023**, *13*, 2346–2368. [[CrossRef](#)]
78. Yan, T.; Su, M.; Wang, Z.; Zhang, J. Second Near-Infrared Plasmonic Nanomaterials for Photoacoustic Imaging and Photothermal Therapy. *Small* **2023**, *19*, 2300539. [[CrossRef](#)]
79. Jia, X.; Xu, W.; Ye, Z.; Wang, Y.; Dong, Q.; Wang, E.; Li, D.; Wang, J. Functionalized Graphene@Gold Nanostar/Lipid for Pancreatic Cancer Gene and Photothermal Synergistic Therapy under Photoacoustic/Photothermal Imaging Dual-Modal Guidance. *Small* **2020**, *16*, 2003707. [[CrossRef](#)]
80. Baipaywad, P.; Ryu, N.; Im, S.S.; Lee, U.; Son, H.B.; Kim, W.J.; Park, H. Facile preparation of poly(N-isopropylacrylamide)/graphene oxide nanocomposites for chemo-photothermal therapy. *Des. Monomers Polym.* **2022**, *25*, 245–253. [[CrossRef](#)]
81. Guo, X.; Mei, J.; Zhang, C. Development of Drug Dual-Carriers Delivery System with Mitochondria-Targeted and pH/Heat Responsive Capacity for Synergistic Photothermal-Chemotherapy of Ovarian Cancer. *Int. J. Nanomed.* **2020**, *15*, 301–313. [[CrossRef](#)]

82. Wu, J.; Wang, M.; Pan, Y.; Pang, Y.; Tang, Y.; Song, C.; Zhu, J.; Zhang, X.; Huang, Q. Synthesis of manganese-oxide and palladium nanoparticles co-decorated polypyrrole/graphene oxide (MnO₂@Pd@PPy/GO) nanocomposites for anti-cancer treatment. *RSC Adv.* **2022**, *12*, 23786–23795. [[CrossRef](#)] [[PubMed](#)]
83. Guo, W.; Chen, Z.; Feng, X.; Shen, G.; Huang, H.; Liang, Y.; Zhao, B.; Li, G.; Hu, Y. Graphene oxide (GO)-based nanosheets with combined chemo/photothermal/photodynamic therapy to overcome gastric cancer (GC) paclitaxel resistance by reducing mitochondria-derived adenosine-triphosphate (ATP). *J. Nanobiotechnol.* **2021**, *19*, 146. [[CrossRef](#)]
84. Romero, M.P.; Buzza, H.H.; Stringasci, M.D.; Estevão, B.M.; Silva, C.C.C.; Pereira-da-Silva, M.A.; Inada, N.M.; Bagnato, V.S. Graphene Oxide Theranostic Effect: Conjugation of Photothermal and Photodynamic Therapies Based on an in vivo Demonstration. *Int. J. Nanomed.* **2021**, *16*, 1601–1616. [[CrossRef](#)]
85. Choi, H.W.; Lim, J.H.; Kim, C.W.; Lee, E.; Kim, J.-M.; Chang, K.; Chung, B.G. Near-Infrared Light-Triggered Generation of Reactive Oxygen Species and Induction of Local Hyperthermia from Indocyanine Green Encapsulated Mesoporous Silica-Coated Graphene Oxide for Colorectal Cancer Therapy. *Antioxidants* **2022**, *11*, 174. [[CrossRef](#)] [[PubMed](#)]
86. Georgieva, M.; Gospodinova, Z.; Keremidarska-Markova, M.; Kamenska, T.; Gencheva, G.; Krasteva, N. PEGylated Nanographene Oxide in Combination with Near-Infrared Laser Irradiation as a Smart Nanocarrier in Colon Cancer Targeted Therapy. *Pharmaceutics* **2021**, *13*, 424. [[CrossRef](#)] [[PubMed](#)]
87. He, S.; Li, J.; Chen, M.; Deng, L.; Yang, Y.; Zeng, Z.; Xiong, W.; Wu, X. Graphene Oxide-Template Gold Nanosheets as Highly Efficient Near-Infrared Hyperthermia Agents for Cancer Therapy. *Int. J. Nanomed.* **2020**, *15*, 8451–8463. [[CrossRef](#)]
88. Zhan, X.; Teng, W.; Sun, K.; He, J.; Yang, J.; Tian, J.; Huang, X.; Zhou, L.; Zhou, C. CD47-mediated DTIC-loaded chitosan oligosaccharide-grafted nGO for synergistic chemo-photothermal therapy against malignant melanoma. *Mater. Sci. Eng. C* **2021**, *123*, 112014. [[CrossRef](#)]
89. Céspedes-Valenzuela, D.N.; Sánchez-Rentería, S.; Cifuentes, J.; Gómez, S.C.; Serna, J.A.; Rueda-Gensini, L.; Ostos, C.; Muñoz-Camargo, C.; Cruz, J.C. Novel Photo- and Thermo-Responsive Nanocomposite Hydrogels Based on Functionalized rGO and Modified SIS/Chitosan Polymers for Localized Treatment of Malignant Cutaneous Melanoma. *Front. Bioeng. Biotechnol.* **2022**, *10*, 1–20. [[CrossRef](#)]
90. Lim, D.K.; Barhoumi, A.; Wylie, R.G.; Reznor, G.; Langer, R.S.; Kohane, D.S. Enhanced photothermal effect of plasmonic nanoparticles coated with reduced graphene oxide. *Nano Lett.* **2013**, *13*, 4075–4079. [[CrossRef](#)]
91. Anichini, C.; Samori, P. Graphene-Based Hybrid Functional Materials. *Small* **2021**, *17*, 2100514. [[CrossRef](#)] [[PubMed](#)]
92. Liu, R.; Zhang, H.; Zhang, F.; Wang, X.; Liu, X.; Zhang, Y. Polydopamine doped reduced graphene oxide/mesoporous silica nanosheets for chemo-photothermal and enhanced photothermal therapy. *Mater. Sci. Eng. C* **2019**, *96*, 138–145. [[CrossRef](#)]
93. Huang, C.; Hu, X.; Hou, Z.; Ji, J.; Li, Z.; Luan, Y. Tailored graphene oxide-doxorubicin nanovehicles via near-infrared dye-lactobionic acid conjugates for chemo-photothermal therapy. *J. Colloid Interface Sci.* **2019**, *545*, 172–183. [[CrossRef](#)] [[PubMed](#)]
94. Zhen, S.J.; Wang, T.T.; Liu, Y.X.; Wu, Z.L.; Zou, H.Y.; Huang, C.Z. Reduced graphene oxide coated Cu_{2-x}Se nanoparticles for targeted chemo-photothermal therapy. *J. Photochem. Photobiol. B Biol.* **2018**, *180*, 9–16. [[CrossRef](#)] [[PubMed](#)]
95. Yang, J.; Xia, X.; He, K.; Zhang, M.; Qin, S.; Luo, M.; Wu, L. Green synthesis of reduced graphene oxide (RGO) using the plant extract of *Salvia spinosa* and evaluation of photothermal effect on pancreatic cancer cells. *J. Mol. Struct.* **2021**, *1245*, 131064. [[CrossRef](#)]
96. Wu, J.; Li, Z.; Li, Y.; Pettitt, A.; Zhou, F. Photothermal Effects of Reduced Graphene Oxide on Pancreatic Cancer. *Technol. Cancer Res. Treat.* **2018**, *17*, 1–7. [[CrossRef](#)]
97. Wang, Z.; Sun, X.; Huang, T.; Song, J.; Wang, Y. A Sandwich Nanostructure of Gold Nanoparticle Coated Reduced Graphene Oxide for Photoacoustic Imaging-Guided Photothermal Therapy in the Second NIR Window. *Front. Bioeng. Biotechnol.* **2020**, *8*, 1–10. [[CrossRef](#)]
98. Hao, L.; Song, H.; Zhan, Z.; Lv, Y. Multifunctional Reduced Graphene Oxide-Based Nanoplatfor for Synergistic Targeted Chemo-Photothermal Therapy. *ACS Appl. Bio Mater.* **2020**, *3*, 5213–5222. [[CrossRef](#)]
99. Lv, C.; Kang, W.; Liu, S.; Yang, P.; Nishina, Y.; Ge, S.; Bianco, A.; Ma, B. Growth of ZIF-8 Nanoparticles In Situ on Graphene Oxide Nanosheets: A Multifunctional Nanoplatfor for Combined Ion-Interference and Photothermal Therapy. *ACS Nano* **2022**, *16*, 11428–11443. [[CrossRef](#)]
100. Schneider, M.G.M.; Martín, M.J.; Otarola, J.; Vakarelska, E.; Simeonov, V.; Lassalle, V.; Nedyalkova, M. Biomedical Applications of Iron Oxide Nanoparticles: Current Insights Progress and Perspectives. *Pharmaceutics* **2022**, *14*, 204. [[CrossRef](#)]
101. Jiang, Z.; Jiang, Z.; Jiang, Y.; Cheng, Y.; Yao, Q.; Chen, R.; Kou, L. Fe-involved nanostructures act as photothermal transduction agents in cancer photothermal therapy. *Colloids Surf. B Biointerfaces* **2023**, *228*, 113438. [[CrossRef](#)] [[PubMed](#)]
102. Chiu, W.-J.; Chen, Y.-C.; Huang, C.-C.; Yang, L.; Yu, J.; Huang, S.-W.; Lin, C.-H. Iron Hydroxide/Oxide-Reduced Graphene Oxide Nanocomposite for Dual-Modality Photodynamic and Photothermal Therapy In Vitro and In Vivo. *Nanomaterials* **2021**, *11*, 1947. [[CrossRef](#)] [[PubMed](#)]
103. Lu, Y.J.; Lin, P.Y.; Huang, P.H.; Kuo, C.Y.; Shalumon, K.T.; Chen, M.Y.; Chen, J.P. Magnetic graphene oxide for dual targeted delivery of doxorubicin and photothermal therapy. *Nanomaterials* **2018**, *8*, 193. [[CrossRef](#)] [[PubMed](#)]
104. Chu, M.; Shao, Y.; Peng, J.; Dai, X.; Li, H.; Wu, Q.; Shi, D. Near-infrared laser light mediated cancer therapy by photothermal effect of Fe₃O₄ magnetic nanoparticles. *Biomaterials* **2013**, *34*, 4078–4088. [[CrossRef](#)]
105. Dash, B.S.; Lu, Y.-J.; Chen, H.-A.; Chuang, C.-C.; Chen, J.-P. Magnetic and GRPR-targeted reduced graphene oxide/doxorubicin nanocomposite for dual-targeted chemo-photothermal cancer therapy. *Mater. Sci. Eng. C* **2021**, *128*, 112311. [[CrossRef](#)]

106. Shakerian Ardakani, T.; Meidanchi, A.; Shokri, A.; Shakeri-Zadeh, A. Fe₃O₄@Au/reduced graphene oxide nanostructures: Combinatorial effects of radiotherapy and photothermal therapy on oral squamous carcinoma KB cell line. *Ceram. Int.* **2020**, *46*, 28676–28685. [[CrossRef](#)]
107. Barrera, C.C.; Groot, H.; Vargas, W.L.; Narváez, D.M. Efficacy and Molecular Effects of a Reduced Graphene Oxide/Fe₃O₄ Nanocomposite in Photothermal Therapy Against Cancer. *Int. J. Nanomed.* **2020**, *15*, 6421–6432. [[CrossRef](#)]
108. Soysal, F.; Çıplak, Z.; Getiren, B.; Gökalp, C.; Yıldız, N. Synthesis and characterization of reduced graphene oxide-iron oxide-polyaniline ternary nanocomposite and determination of its photothermal properties. *Mater. Res. Bull.* **2020**, *124*, 110763. [[CrossRef](#)]
109. Du, B.; Liu, J.; Ding, G.; Han, X.; Li, D.; Wang, E.; Wang, J. Positively charged graphene/Fe₃O₄/polyethylenimine with enhanced drug loading and cellular uptake for magnetic resonance imaging and magnet-responsive cancer therapy. *Nano Res.* **2017**, *10*, 2280–2295. [[CrossRef](#)]
110. Ramezani Farani, M.; Khadiv-Parsi, P.; Riazi, G.H.; Shafiee Ardestani, M.; Saligheh Rad, H. PEGylation of graphene/iron oxide nanocomposite: Assessment of release of doxorubicin, magnetically targeted drug delivery and photothermal therapy. *Appl. Nanosci.* **2020**, *10*, 1205–1217. [[CrossRef](#)]
111. Gong, T.; Wang, X.; Ma, Q.; Li, J.; Li, M.; Huang, Y.; Liang, W.; Su, D.; Guo, R. Triformyl cholic acid and folic acid functionalized magnetic graphene oxide nanocomposites: Multiple-targeted dual-modal synergistic chemotherapy/photothermal therapy for liver cancer. *J. Inorg. Biochem.* **2021**, *223*, 111558. [[CrossRef](#)] [[PubMed](#)]
112. Zhang, Y.; Li, J.; Pu, K. Recent advances in dual- and multi-responsive nanomedicines for precision cancer therapy. *Biomaterials* **2022**, *291*, 121906. [[CrossRef](#)] [[PubMed](#)]

Disclaimer/Publisher's Note: The statements, opinions and data contained in all publications are solely those of the individual author(s) and contributor(s) and not of MDPI and/or the editor(s). MDPI and/or the editor(s) disclaim responsibility for any injury to people or property resulting from any ideas, methods, instructions or products referred to in the content.